International Journal of Solids and Structures 250 (2022) 111704

Contents lists available at ScienceDirect

International Journal of Solids and Structures

journal homepage: www.elsevier.com/locate/ijsolstr

Adding multi-material regions embracing the tip leads to significant capacity increase in structures weakened by V-notches under antiplane shear and torsion

Marco Salviato

William E. Boeing Department of Aeronautics and Astronautics, University of Washington, Seattle, WA 98195, USA

ARTICLE INFO

Keywords:
Antiplane shear
Complex potentials
Composites
Closed-form solutions
Notch Stress Intensity Factors

ABSTRACT

This study investigates how the insertion of multimaterial circular regions embracing the tip of a finite V-notch can be used to reduce the Notch Stress Intensity Factors (NSIFs) in structures subjected to antiplane shear or torsion. Towards this goal, this work presents a novel theoretical framework to calculate stress distributions and NSIFs in closed-form. Thanks to the new solution, it is shown that by tuning multimaterial region radii and elastic properties it is possible to significantly reduce the NSIFs and stress concentrations at the material interfaces.

To investigate whether the proposed multimaterial system translates into increased structural capacity even in the presence of significant nonlinear deformations, computational simulations were conducted using nonlinear hyperelastic-damage and elasto-plastic-damage models. The preliminary results show increases of structural capacity up to 46% and of nominal strain at failure of up to 86% at the expenses of only a 8% reduction in structural stiffness.

It is expected that a similar approach can be extended to other loading conditions (e.g. mode I and mode II, and fatigue) and that even larger gains can be obtained by performing thorough optimization studies.

1. Introduction

The advent of multimaterial additive manufacturing has given researchers and designers the opportunity to explore unprecedented ways to increase the damage tolerance of structural components (Bandyopadhyay and Heer, 2018; Rafiee et al., 2020). Ubaid et al. (2018), for instance, investigated multimaterial jetting additive manufacturing to realize strength and performance enhancement of multilayered materials by spatial tailoring of adherend compliance and morphology. Compared to the baseline homogeneous system, they were able to obtain an increase of strength by 20%, toughness by 48%, and strain at failure by 18%.

Lin et al. (2014) leveraged multimaterial additive manufacturing to explore the mechanical behavior of suture interfaces inspired by the intricate, hierarchical designs of ammonites. They showed that proper combinations of soft and hard materials along with proper selection of the order of hierarchy of the interface can lead to significant stiffness, tensile strength, and toughness compared to conventional interfaces.

Suksangpanya et al. (2018) used multimaterial additive manufacturing to reproduce the Bouligand structure present in the dactyl club of the smashing mantis shrimp. Leveraging experiments on three-point bend specimens and semi-analytical modeling, they showed that, thanks to changes in local fracture mode and increases in crack surface area, the initiation fracture toughness can be increased almost twofold while the fracture toughness at catastrophic failure can be increased of an order of magnitude. Zaheri et al. (2018) showed that similar microstructures are the secrets for the outstanding stiffness and toughness of the cuticle of the figeater beetle (*Cotinis mutabilis*).

Raney et al. (2018) developed a novel rotational 3D printing method that enables spatially controlled orientation of short fibers in polymer matrices by varying the nozzle rotation speed relative to the printing speed. Using this technology, they fabricated carbon fiber–epoxy composites composed of volume elements with defined fiber arrangements. By tailoring the fiber orientation in select areas, the authors were able to demonstrate the possibility of increasing damage tolerance and capacity of several structural components.

Martin et al. (2015) proposed a new additive manufacturing technology called "3D magnetic printing" that is capable of printing dense ceramic/polymer composites in which the direction of the ceramic-reinforcing particles can be finely tuned. Thanks to this new method, the authors explored the mechanics of complex bioinspired reinforcement architectures showing the possibility of steering cracks using controlled mesostructures and increase damage tolerance.

E-mail address: salviato@aa.washington.edu.

https://doi.org/10.1016/j.ijsolstr.2022.111704
Received 29 November 2021; Received in revised form 12 April 2022; Accepted 11 May 2022
Available online 19 May 2022

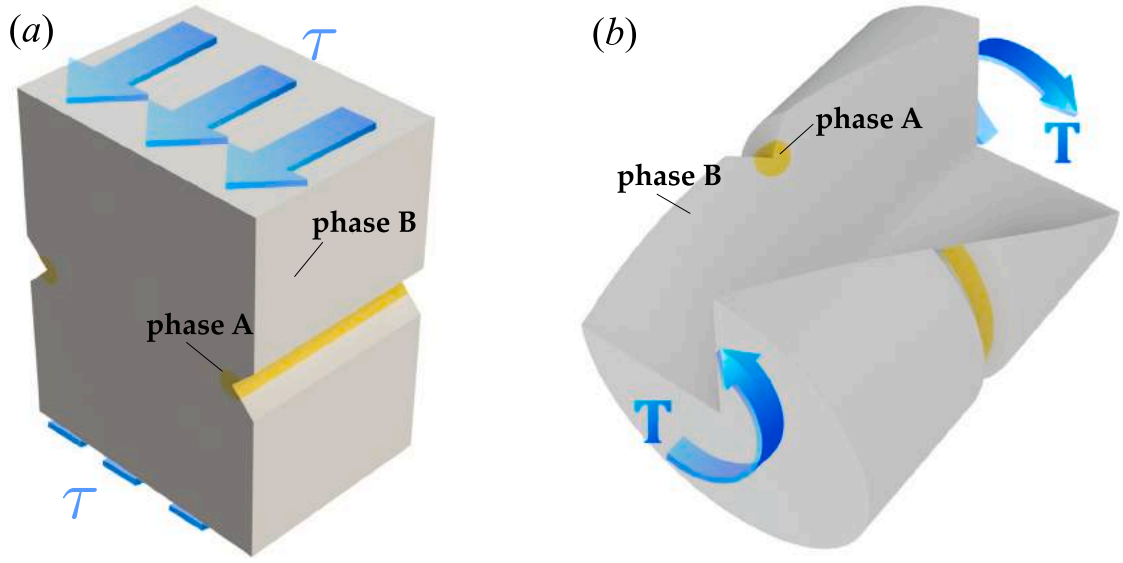

Fig. 1. Examples of the systems investigated in this work: (a) component under antiplane shear and (b) three-quarter section view of a circular shaft under torsion. Both systems are weakened by a V-notch featuring a circular region made of a different material embracing the tip.

Leveraging 3D printing of continuous carbon fiber composites Sugiyama et al. (2020) investigated the optimization of curved fiber trajectories to realize variable fiber volume fraction and stiffness composites to increase the capacity of composite structures. They were able to show that proper selection of the fiber paths can increase the ratio between the structural capacity and its overall weight of almost 60% compared to traditional designs. Using a novel isogeometric computational framework Suzuki et al. (2021) showed that the stress concentration factor of notched additively manufactured composites can be reduced to almost half without affecting the structural stiffness.

Inspired by the foregoing recent advances in additive manufacturing, this work aims at exploring the use of multimaterial configurations to increase the capacity and toughness of V-notched structural components under antiplane shear or torsion. In fact, several structural engineering components including e.g. power transmission shafts for automotive or wind energy, levers, springs, brackets, and screws for power transmission are subjected to antiplane shear or torsion as the predominant loading conditions. In such components, geometrical variations are ubiquitous. These lead to the presence of notches -such as the finite V-notch- and grooves which may lead to crack formation and final failure. The idea explored in this study and shown in Fig. 1(a,b) is to investigate the addition at the tip of the notch of multiple circular regions made of different material combinations to reduce the Notch Stress Intensity Factor (NSIF) (Gross and Mendelson, 1972) and promote higher energy dissipation by plastic deformations. The goal is to increase the resistance to fracture thus improving the structural performance of these important engineering components.

In pursuit of this goal, the problem is initially investigated within the framework of Linear Elastic Fracture Mechanics (LEFM) to determine the effects of the material properties and notch configuration on the NSIF. Recently, significant studies have investigated the stress field and stress intensity factors in multimaterial structures under antiplane shear and torsion. Leveraging a complex potential approach Zappalorto and Salviato (2019) developed closed form and approximate solutions to describe the antiplane shear stress distribution in orthotropic plates with lateral blunt notches. They later extended this approach for the case of in-plane shear loading (Pastrello et al., 2022).

Salviato et al. (2018) and Zappalorto et al. (2019) investigated the mode III stress distribution ahead of cracks initiated at sharp and blunt notch tips. They were able to provide closed form solutions for the calculation of the Stress Intensity Factors (SIF) for a number of notch configurations.

However, notwithstanding the efforts devoted in the past decades, a theoretical framework for the calculation of the displacement and stress distributions for multimaterial V-notches as the ones shown in Fig. 1(a,b) is still elusive. This is the topic of the first part of the present study in which, combining conformal mapping and complex potentials, a new general method for calculating the stress distribution in such multimaterial systems in closed form is presented. Thanks to the proposed theoretical framework, the present study investigates the effects of the material properties and region radii on the NSIF providing clear guidelines for the mitigation of the stress intensity at the notch and the stress concentration at the material interfaces. It is worth mentioning here that such theoretical framework is key to fully understand how the geometrical and material parameters of the problem affect the process of failure and to build on this knowledge to investigate more complex configurations numerically. The understanding obtained via analytical solutions of a simple representative problem is way deeper than any computational simulation. In fact, closed-form solutions provide an explicit description of the fundamental relationships describing the problem while computational modeling only provides a mean to perform experiments "virtually" but does not provide the researcher with a final law synthesizing the results. Only after shedding light to the physical laws of a simple-yet-representative problem such as the one presented in this work can one leverage this knowledge to investigate more complex configurations numerically and to obtain a proper comprehension of the problem.

Finally, in the second part of the study, advanced elastoplastic-damage and hyperelastic-damage models are implemented to investigate the efficacy of the proposed multimaterial system even in the presence of significant inelastic strains which are likely to occur under the investigated loading conditions. The results confirm that the concept of multimaterial notch blunting can lead to significant reductions of the NSIF, which translates into higher structural capacity and toughness.

The article is organized as follows. Section 2 presents a novel general theoretical framework for the analytical solution of the stress field in multimaterial domains subject to antiplane shear and torsion. Section 3 discusses the application of the approach to the case of a bimaterial system. It provides closed form solutions for stresses, NSIFs, and displacement as function of the geometrical configuration of the notch and the elastic properties of the materials. Section 4 presents the application of the theoretical framework to the case of a trimaterial

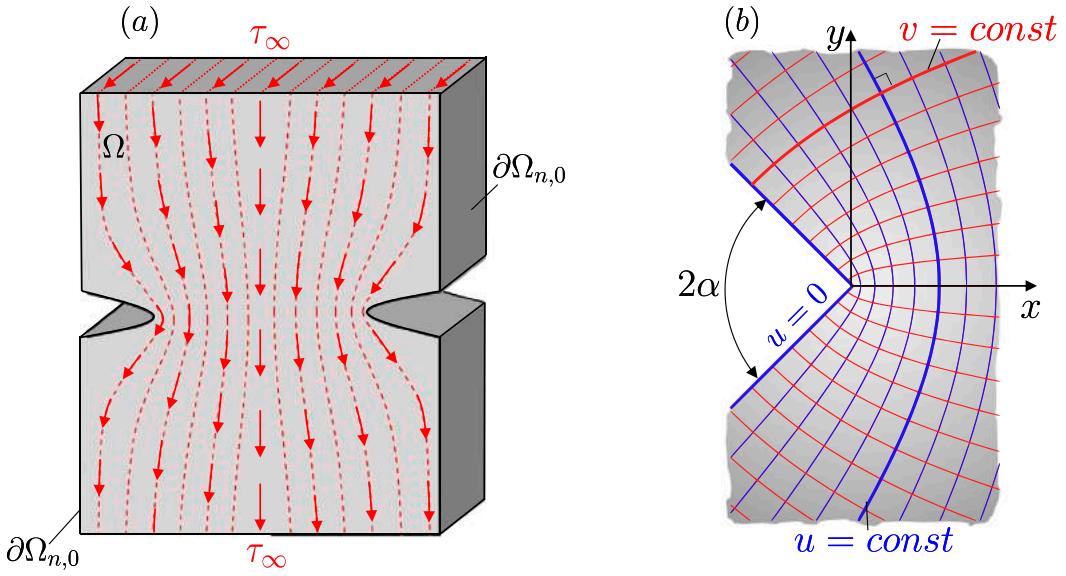

Fig. 2. (a) 2D domain $\Omega \cup \partial\Omega$ subjected to a remote antiplane shear stress τ_∞ and (b) example of the conformal transformation $z = \xi^q$ with $q = 2(\pi - \alpha)/\pi$ and $\xi = u + iv$ typically used for the description of deep hyperbolic notches (Neuber, 1958a,b).

configuration. Several contour plots are presented to discuss the complex influence on the NSIF of the radii of the regions and their elastic properties. Section 5 discusses the implementation of elastoplastic-damage and hyperelastic-damage models for the nonlinear simulation of torsion in bimaterial system composed of vulcanized rubber and epoxy. The models allow to capture the plastic deformation close to the notch tip and enable the evaluation of the effectiveness of the proposed multimaterial system in the presence of realistic deformations. The manuscript ends with Section 6 where a thorough analysis of the main conclusions of this work is presented.

2. Unified solution for the stress fields in antiplane shear and torsion problems in multi-material domains

2.1. Governing equations in isotropic and homogeneous media

Let us consider first a semi-infinite 2D domain $\Omega \cup \partial\Omega$ made of a isotropic and homogeneous material featuring a linear elastic behavior and assume that the domain is subjected to a remote antiplane shear stress τ_∞ Fig. 2(a). Considering the Cartesian coordinate system (x, y, z) defined in Fig. 2b, the equilibrium equation assuming the absence of body forces can be written as follows:

$$\frac{\partial \tau_{zx}}{\partial x} + \frac{\partial \tau_{zy}}{\partial y} = 0 \tag{1}$$

where $\tau_{zi}(i = x, y)$ = shear stress components in $x-$ and $y-$ directions. The shear stress components are linked to the engineering shear strains through Hooke's law: $\tau_{zi} = 1/G\gamma_{zi}(i = x, y)$ where G represents the elastic shear modulus of the material. Introducing the kinematic relationships, the stresses can be written as a function of the displacement in the z-direction, w: $\tau_{zx} = G\partial w/\partial x$ and $\tau_{zy} = G\partial w/\partial y$. Then, if one substitutes the foregoing expressions into Eq. (1), the governing equation in terms of the displacement becomes a two-dimensional Laplace equation:

$$\nabla^2 w = 0 \tag{2}$$

where $\nabla^2 = \partial^2/\partial x^2 + \partial^2/\partial y^2$ = the laplacian operator.

The solution of Eq. (2) in the two-dimensional domain $\Omega \cup \partial\Omega$ in the presence of Dirichlet or von Neumann boundary conditions on $\partial\Omega$ can be particularly cumbersome except for cases in which the domain is simple. To overcome this problem, it is convenient to leverage conformal mapping to transform the complex domain in one for which it is easier to apply the boundary conditions. Conformal maps can be described by complex analytic functions (Fisher, 1999; Brown and Churchill, 2009) so that the change of coordinates takes the form: $z = z(\xi)$ with $z = x + iy$ and $\xi = u + iv$. It can be shown that the transformation is always bijective and satisfies the Cauchy–Riemann (C–R) conditions $\partial u/\partial x = \partial v/\partial y$, $\partial u/\partial y = -\partial v/\partial x$ in Ω. Since the Laplace equation is conformally invariant, the advantage of using a conformal map is that the governing equation in the new coordinates takes the same form as the one in Cartesian coordinates:

$$\frac{\partial^2 w}{\partial u^2} + \frac{\partial^2 w}{\partial v^2} = 0 \tag{3}$$

while making it easier to apply the boundary conditions (Fisher, 1999; Brown and Churchill, 2009). The curvilinear stress components in the new coordinate system can be calculated as follows:

$$\tau_{zu} = \frac{G}{h}\frac{\partial w}{\partial u}, \qquad \tau_{zv} = \frac{G}{h}\frac{\partial w}{\partial v} \tag{4}$$

where $h = h_u = \sqrt{(\partial x/\partial u)^2 + (\partial y/\partial u)^2} = h_v = \sqrt{(\partial x/\partial v)^2 + (\partial y/\partial v)^2}$ are the metric coefficients of the transformation (Sokolnikoff, 1956).

Salviato and Zappalorto (2016) showed that a significant simplification to the solution can be provided by considering conformal maps in which the condition $v = v_0$ (with v_0 being a real constant) describes the portion of boundary, $\partial\Omega_{n,0}$, where the shear stress normal to the boundary is null: $\tau_{zn} = 0$. In fact, in such a case:

$$w = Au \tag{5}$$

and the curvilinear stress components can be calculated as follows:

$$\tau_{zu} = \frac{\psi}{\|z'(\xi)\|}, \qquad \tau_{zv} = 0 \tag{6}$$

where $\|z'(\xi)\| = h$ is the magnitude of the first derivative of the conformal map and $\psi = AG$ is a constant to be determined by imposing the remote stress conditions. Then, the expression for the Cartesian stress components takes the following form (Salviato and Zappalorto, 2016):

$$\tau_{zx} - i\tau_{zy} = \psi\frac{\mathrm{d}\xi(z)}{\mathrm{d}z} \tag{7}$$

The mathematical proof in support of the foregoing equations can be found in Salviato and Zappalorto (2016) or Salviato and Phenisee (2019) where a similar framework was used to solve problems in electrostatics.

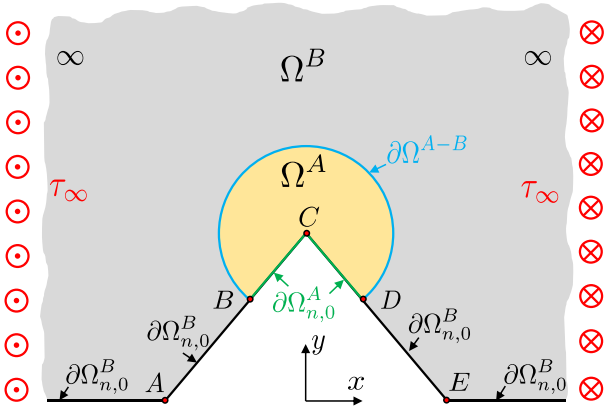

Fig. 3. Example of semi-infinite domain $\Omega = \Omega^A \cup \Omega^B$ with a finite notch featuring one or more regions of different materials surrounding the tip. The $\tau_{zn} = 0$ condition is applied to $\Omega^A_{n,0}$ and $\Omega^B_{n,0}$ for regions A and B respectively. Ω^{A-B} represents the interface between regions A and B.

2.2. Governing equations for notches featuring multi-material regions embracing the tip

In this work, we seek to develop a new solution for the antiplane shear stress field for notches featuring multi-material regions embracing the tip (Fig. 3). In fact, expressions linking the geometrical and material parameters to the stress distribution and related Notch Stress Intensity Factors (NSIFs) are still elusive.

With reference to Fig. 3, let regions Ω^A and Ω^B be made of different linear elastic materials featuring shear elastic moduli G_A and G_B respectively. Let $\partial\Omega^A_{n,0}$ and $\partial\Omega^B_{n,0}$ be the portions of boundary subjected to no stresses for regions Ω^A and Ω^B respectively while $\partial\Omega^{A-B}$ represents the interface boundary between the two regions. Let also w_A and w_B be the displacement components in the $z-$direction in regions Ω^A and Ω^B respectively.

Taken singularly, each region can be considered as homogeneous. Hence, the same governing equation for homogeneous materials, Eq. (2), can be applied to each region separately. Accordingly, the system of equations to be solved reads:

$$\begin{cases} \nabla^2 w_A = 0, & \text{for } (x,y) \in \Omega^A & \text{(a)} \\ \tau^A_{zn} = 0, & \text{for } (x,y) \in \partial\Omega^A_{n,0} & \text{(b)} \\ \nabla^2 w_B = 0, & \text{for } (x,y) \in \Omega^B & \text{(c)} \\ \tau^B_{zn} = 0, & \text{for } (x,y) \in \partial\Omega^B_{n,0} & \text{(d)} \\ \tau^A_{zn} = \tau^B_{zn}, & \text{for } (x,y) \in \partial\Omega^{A-B} & \text{(e)} \\ w_A = w_B, & \text{for } (x,y) \in \partial\Omega^{A-B} & \text{(f)} \end{cases} \tag{8}$$

where Eqs. (8)(b), (8)(d), and (8)(e) represent equilibrium conditions on the boundaries and Eq. (8)(f) guarantees the compatibility of the displacement field. This latter condition, along with Eq. (8)(e), is necessary since $\Omega = \Omega^A \cup \Omega^B$ is not homogeneous.

The solution of the foregoing system of equations can be generalized and significantly simplified by taking advantage of proper conformal maps as described next.

2.3. General solution framework

The new solution presented in this work relies on the use of a set of conformal maps describing each multimaterial region. Let us consider two conformal mappings $z = z(\xi_v)$ and $z = z(\xi)$ with $\xi_v = u_v + iv_v$ and $\xi = u + iv$. The two maps are defined so that the condition $v_v = v_{v,0}$ describes $\partial\Omega^A_{n,0} \cup \partial\Omega^B_{n,0}$ while $v = v_0$ describes $\partial\Omega^B_{n,0} \cup \partial\Omega^{A-B}$ (see Fig. 3). Furthermore, the complex function $\xi_v = p(\xi)$ defining the relation between the two curvilinear variables is an analytic function. Taking advantage of the proposed conformal maps, the system of governing Eqs. (8)(a)–(8)(f) can be significantly simplified as follows:

$$\begin{cases} \dfrac{\partial^2 w_A}{\partial u_v^2} + \dfrac{\partial^2 w_A}{\partial v_v^2} = 0, & \text{for } \xi_v \in (-\infty,\infty) \times [v_{v,0},\infty) & \text{(a)} \\ \dfrac{\partial w_A}{\partial v_v} = 0, & \text{for } v_v = v_{v,0} & \text{(b)} \\ \dfrac{\partial^2 w_B}{\partial u^2} + \dfrac{\partial^2 w_B}{\partial v^2} = 0, & \text{for } \xi \in (-\infty,\infty) \times [v_0,\infty) & \text{(c)} \\ \dfrac{\partial w_B}{\partial v} = 0, & \text{for } v = v_0 & \text{(d)} \\ G_A \dfrac{\partial \omega_A}{\partial v} = G_B \dfrac{\partial w_B}{\partial v}, & \text{for } \xi \in \partial\Omega^{A-B} & \text{(e)} \\ \omega_A = w_B, & \text{for } \xi \in \partial\Omega^{A-B} & \text{(f)} \end{cases} \tag{9}$$

where $\omega_A(u,v) = w_A[u_v(u,v), v_v(u,v)]$ represents the displacement in region Ω^A written as a function of the curvilinear coordinates u, v.

For the solution of Eqs. (9)(a)–(9)(f) one can note that an easy way to satisfy compatibility, Eq. (9)(f), and Eqs. (9)(a)–(9)(d) at the same time would be to extend the solution for Ω^A to Ω^B (subproblem 1 in Fig. 4). In fact, let $w_A = w_A(u_v, v_v)$ satisfy Eqs. (9)(a) and (9)(b). Then, as composed function of two harmonic functions, $w_B = \omega_A(u,v) = w_A[u_v(u,v), v_v(u,v)]$ would be harmonic in ξ. Considering the definitions of ξ_v and ξ, this means that w_B would also satisfy both Eqs. (9)(c) and (9)(d). However, a simple extension would not be enough to fulfill the equilibrium condition, Eq. (9)(e), on the interface Ω^{A-B} which also depends on the elastic properties of each region. To solve this problem, the solution for the displacement in Ω^B must be augmented by an additional term. Such term should still satisfy the equilibrium condition in $\partial\Omega^B_{n,0}$. A natural choice is to use Bu since it automatically satisfies the condition that $\partial(Bu)/\partial v = 0$ in $\partial\Omega^B_{n,0}$. It is interesting to note that, following the derivations presented in Section 2.1, Bu would be the solution for the displacement field in region B if region A were eliminated and the same remote boundary conditions were applied (subproblem 2 in Fig. 4).

Following Eq. (5), it is easy to derive the expression for the displacement w in $\Omega = \Omega^A \cup \Omega^B$:

$$w = \begin{cases} w_A(u_v, v_v) = Cu_v, & \text{for } \xi_v \in \Omega^A & \text{(a)} \\ w_B(u,v) = A\omega_A(u,v) + Bu = Au_v(u,v) + Bu, & \text{for } \xi \in \Omega^B & \text{(b)} \end{cases} \tag{10}$$

where A, B, C are real constants to be determined by imposing the remote stress, and the equilibrium and compatibility conditions on the interface. Finally, leveraging Eq. (7), the Cartesian components of the stresses can be calculated by taking the real and imaginary parts of the following equation:

$$\tau_{zx} - i\tau_{zy} = \begin{cases} CG_A \dfrac{\mathrm{d}\xi_v(z)}{\mathrm{d}z}, & \text{for } \xi_v \in \Omega^A & \text{(a)} \\ G_B \left[A \dfrac{\mathrm{d}\xi_v(z)}{\mathrm{d}z} + B \dfrac{\mathrm{d}\xi(z)}{\mathrm{d}z} \right], & \text{for } \xi \in \Omega^B & \text{(b)} \end{cases} \tag{11}$$

In summary, the displacement and stress distributions in multi-material domains as the one shown in Fig. 3 can be obtained by performing the following three-step procedure (Fig. 4):

Step 1: Using the analytical approach described in Section 2.1, find the solutions for the displacement and stress distributions underlain by the transformations $z = z(\xi_v)$ and $z = z(\xi)$ (subproblems 1 and 2 in Fig. 4).

Step 2: Find the general solution for the displacement of the original problem, defined except for the constants A, B, and C, by combining the solutions of the subproblems, Eqs. (9)(a)–(9)(f) (see Fig. 4, Step 2). Then, calculate the stress distribution leveraging Eqs. (11)(a) and (11)(b).

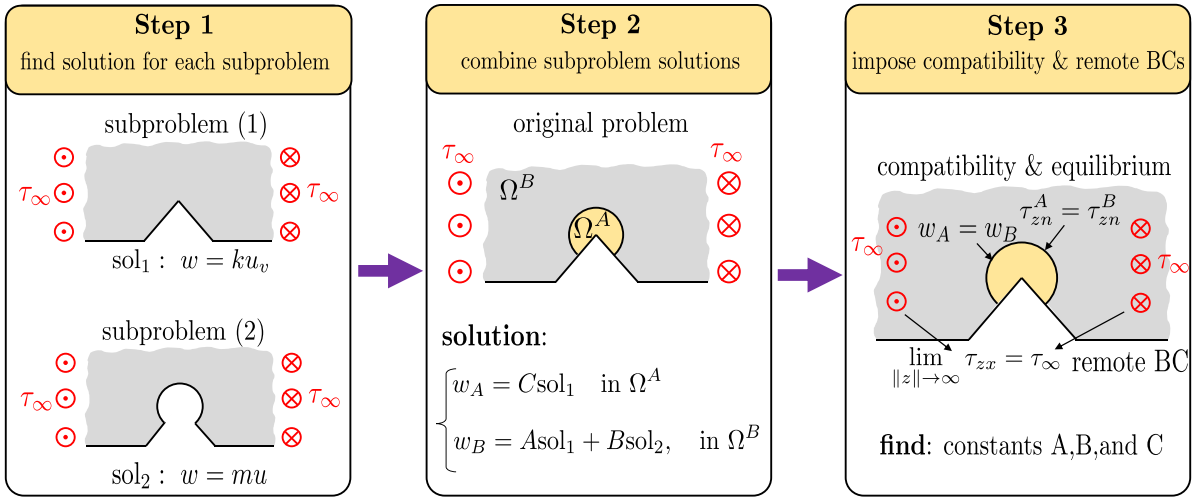

Fig. 4. Flowchart summarizing the three-step strategy for calculating the stress distribution. Step 1 requires the calculation of the stresses for the subproblems defined by the transformations $z = z(\xi_v)$ and $z = z(\xi)$. In Step 2, the general solution of the original problem is obtained as a combination of the subproblem solutions. Finally, in Step 3, the final solution is uniquely defined by imposing the equilibrium and compatibility conditions on the interface, and the remote conditions.

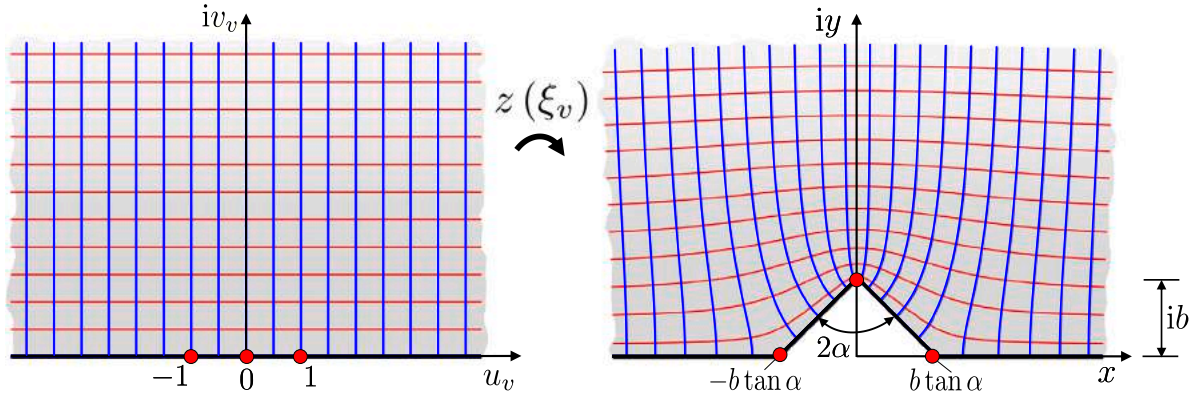

Fig. 5. Conformal map, Eq. (12), transforming the upper half plane, $v_v \geq 0$ into a semi-infinite domain weakened by a finite V-notch of depth b and opening angle 2α.

Step 3: Find the values of the constants A, B, and C by imposing compatibility and equilibrium along the interface $\partial\Omega^{A-B}$, and by imposing the remote stress condition: $\lim_{\|z\|\to\infty} \tau_{zx} = \tau_\infty$ (Fig. 4, Step 3).

The application of the general framework to the particular case of a multi-material V-notch as the one shown in Fig. 3 requires the solutions of two subproblems: the *finite V-notch* and the *finite V-notch with a circular end hole* (see Fig. 4, Step 1). Such solutions are derived in the next sections for the first time.

2.4. Finite V-notch

As discussed in the previous sections, the solution for the displacement and shear stress distributions for the finite V-notch can be easily obtained from Eq. (7) provided that one knows the conformal map $Z = Z(\xi_v)$ transforming the upper half-plane ($v_v \geq 0$) into a semi-infinite plane featuring a finite V-notch (Fig. 5). With reference to the coordinate system shown in Fig. 5, such mapping can be derived leveraging a Schwarz–Christoffel transformation (Driscoll and Trefethen, 2002):

$$Z(\xi) = \frac{A_v \pi \exp\left[i\left(\alpha - \frac{\pi}{2}\right)\right]}{2(\pi - \alpha)} \xi_v^{2\left(1-\frac{\alpha}{\pi}\right)} H(\alpha, \xi_v) + ib \tag{12}$$

where b represents the depth of the V-notch, $2\alpha \in [0, \pi]$ is the notch opening angle, and the boundary featuring zero shear stress components in the normal direction, $\partial\Omega_{n,0}$, is defined by the condition $v_v = 0$ (Fig. 5). Furthermore,

$$A_v = \frac{b\sqrt{\pi}}{\cos\alpha\, \Gamma(1-\alpha/\pi)\, \Gamma(1/2+\alpha/\pi)} \tag{13}$$

is a constant depending on the notch depth b and notch opening angle α with $\Gamma(t) = \int_0^\infty x^{t-1}\exp(-x)\mathrm{d}x$ being the gamma function (Abramowitz and Stegun, 1964). Finally:

$$H(\alpha, \xi_v) = {}_2F_1\left(\frac{1}{2} - \frac{\alpha}{\pi}, 1 - \frac{\alpha}{\pi}, 2 - \frac{\alpha}{\pi}, \xi_v^2\right) \tag{14}$$

where ${}_2F_1(a, b; c; z) = \sum_{k=0}^\infty (a)_k (b)_k / (c)_k z^k / k!$ is the Gaussian hypergeometric function (Andrews et al., 1999; Yoshida, 2013).

Starting from the conformal map, Eq. (12), the Cartesian stress components written as a function of the curvilinear coordinates can be calculated taking advantage of Eq. (7):

$$\tau_{zx} - i\tau_{zy} = \psi \left[\frac{\mathrm{d}Z(\xi_v)}{\mathrm{d}\xi_v}\right]^{-1} = \psi \frac{(\xi_v^2 - 1)^{1/2-\alpha/\pi}}{\xi_v^{1-2\alpha/\pi}} \tag{15}$$

from which one can note that the remote boundary condition gives $\lim_{\|\xi_v\|\to\infty}(\tau_{zx} - i\tau_{zy}) = \psi = \tau_\infty$. Then, the equations for the stress components can be rewritten as a function of the remote stress τ_∞ by extracting the real and imaginary parts of Eq. (15) as follows:

$$\tau_{zx}(u_v, v_v) = \tau_\infty \frac{\left[(u_v^2 - v_v^2 - 1)^2 + 4u_v^2 v_v^2\right]^{1/4-\alpha/2\pi}}{(u_v^2 + v_v^2)^{1/2-\alpha/\pi}} \cos\eta \tag{16}$$

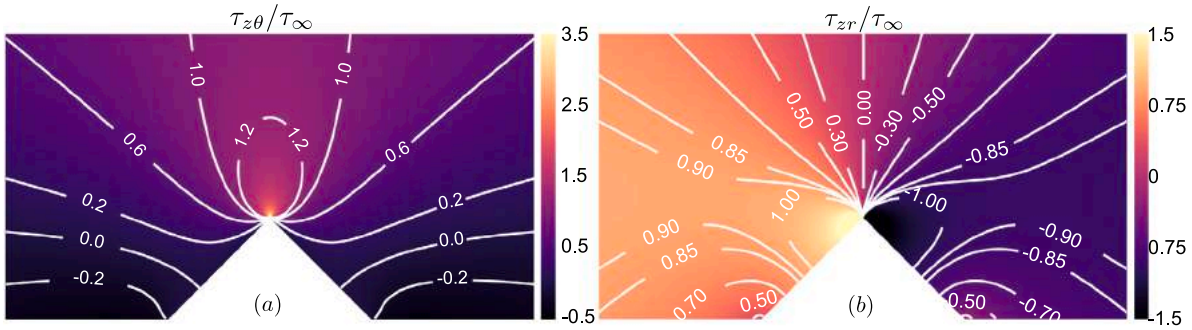

Fig. 6. Normalized stress distribution for a finite V-notch of depth $b = 5$ mm and opening angle $2\alpha = 90°$ subjected to a remote stress $\lim_{z\to\infty} \tau_{zx} = -\tau_\infty$: (a) $\tau_{z\theta}/\tau_\infty$ and (b) τ_{zr}/τ_∞.

$$\tau_{zy}\left(u_v, v_v\right) = \tau_\infty \frac{\left[\left(u_v^2 - v_v^2 - 1\right)^2 + 4u_v^2 v_v^2\right]^{1/4-\alpha/2\pi}}{\left(u_v^2 + v_v^2\right)^{1/2-\alpha/\pi}} \sin\eta \tag{17}$$

where $\eta = (\alpha/\pi - 1/2)\arg\left(u_v^2 - v_v^2 - 1 + 2iu_v v_v\right) + (1 - 2\alpha/\pi)\arg\left(u_v + iv_v\right)$. It is worth mentioning that, leveraging Eqs. (16) and (17), the polar components can be calculated easily: $\tau_{zr} = \cos\theta\tau_{zx} + \sin\theta\tau_{zy}$ and $\tau_{z\theta} = \cos\theta\tau_{zy} - \sin\theta\tau_{zx}$.

Contour plots of the shear stress components calculated by means of Eqs. (16) and (17) are shown in Fig. 6.

2.4.1. Near-tip stress field

The stress distribution described by Eqs. (16) and (17) is written as a function of the curvilinear coordinates u_v and v_v. However, for practical uses, it would be convenient to express the stress components as a function of a Cartesian coordinate system centered at the tip, (x, y), or a polar coordinate system (r, θ). This would require the inversion of the conformal map expressed in Eq. (12): $\xi_v(x, y) = Z^{-1}(x, y)$. However, considering the complexity of the transformation, a closed-form solution would not be attainable. A possible way to overcome this issue is to acknowledge that the failure behavior of the structure will mostly depend on the stress distribution close to the notch tip rather than away from it. Furthermore, for the calculation of the Notch Stress Intensity Factor (NSIF), only the near-tip stress field is of relevance. Accordingly, one can focus on the calculation of the stress components in a region sufficiently close to the tip where significant simplifications can be introduced. In fact, expanding Eq. (12) in Laurent series around $\xi_v = 0$ (which is the condition describing the location of the notch tip), retaining only the linear terms, and substituting into Eq. (15) one can find the following expression for the stresses closed to the tip (Salviato and Zappalorto, 2016):

$$\tau_{zx} - i\tau_{zy} = \tau_\infty \exp\left[i\frac{\pi(q-1)}{2q}\right]\left(\frac{A_v}{q}\right)^{1/q-1} z^{1/q-1} \tag{18}$$

where the equality $2\alpha = \pi(2 - q)$ has been used. Using the foregoing equation, the Notch Stress Intensity Factor (NSIF) (Gross and Mendelson, 1972) can be easily determined leveraging its definition $K_3 = \sqrt{2\pi}\lim_{y\to 0}\tau_{zx}(0, y)\, y^{1-1/q}$ which leads to the following expression:

$$K_3 = \tau_\infty b^{1-1/q} k_3 \tag{19}$$

where:

$$k_3 = \sqrt{2\pi}\left[\frac{\sqrt{\pi}}{q\cos\alpha\,\Gamma\left(1 - \frac{\alpha}{\pi}\right)\Gamma\left(\frac{1}{2} + \frac{\alpha}{\pi}\right)}\right]^{1-1/q} \tag{20}$$

is a dimensionless function depending solely on the notch opening angle. After calculating the NSIF and extracting the real and imaginary parts of Eq. (18), the near-tip Cartesian stress components can be written in polar coordinates as follows:

$$\tau_{zx} = \frac{K_3}{\sqrt{2\pi}r^{1-\frac{1}{q}}}\cos\left[\left(1 - \frac{1}{q}\right)\left(\theta - \frac{\pi}{2}\right)\right] \tag{21}$$

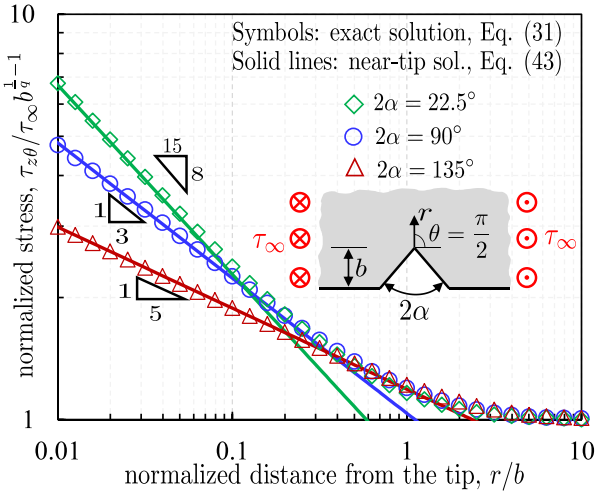

Fig. 7. Double-logarithmic plot showing the normalized stress, $\tau_{z\theta}/\tau_\infty b^{\frac{1}{q}-1}$, as a function of the normalized distance from the notch tip, r/b along the bisector ($\theta = \pi/2$).

$$\tau_{zy} = \frac{K_3}{\sqrt{2\pi}r^{1-\frac{1}{q}}}\sin\left[\left(1 - \frac{1}{q}\right)\left(\theta - \frac{\pi}{2}\right)\right] \tag{22}$$

Finally, leveraging the relationship $\tau_{zr} - i\tau_{z\theta} = \exp(i\theta)\left(\tau_{zx} - i\tau_{zy}\right)$, one can derive the equations for the polar stress components:

$$\tau_{zr} = \frac{K_3}{\sqrt{2\pi}r^{1-\frac{1}{q}}}\cos\left[\frac{1}{q}\left(\frac{\pi}{2} - \theta\right) - \frac{\pi}{2}\right] \tag{23}$$

$$\tau_{z\theta} = \frac{K_3}{\sqrt{2\pi}r^{1-\frac{1}{q}}}\sin\left[\frac{1}{q}\left(\frac{\pi}{2} - \theta\right) - \frac{\pi}{2}\right] \tag{24}$$

Fig. 7 shows the normalized stress, $\|\tau_{z\theta}\|/\tau_\infty b^{\frac{1}{q}-1}$, as a function of the normalized distance from the notch tip along the bisector, r/b, in double-logarithmic scale for various notch opening angles. The symbols represent the exact solution calculated numerically by means of Eq. (16) while the solid lines show the stresses calculated using the near-tip solution, Eq. (24). As can be noted, the stresses feature a singularity of order $1 - 1/q$ with $q = 2 - 2\alpha/\pi$ for $r \to 0$ as abundantly reported in previous literature (Neuber, 1958a,b; Zappalorto et al., 2008). The strength of the singularity increases with decreasing values of the notch opening angle, 2α and takes the maximum value of $1/2$ for the case of a crack, $2\alpha = 0$. Another interesting observation that can be drawn from Fig. 7 is that the near-tip solution, Eq. (24), provides a remarkably good approximation of the exact solution for distances up to one tenth of the notch depth, b. Considering that for brittle materials the size of the Fracture Process Zone (FPZ) is generally considerably smaller than typical notch depths, the use of the near-tip solution for the application of failure criteria is more than justified. The same holds

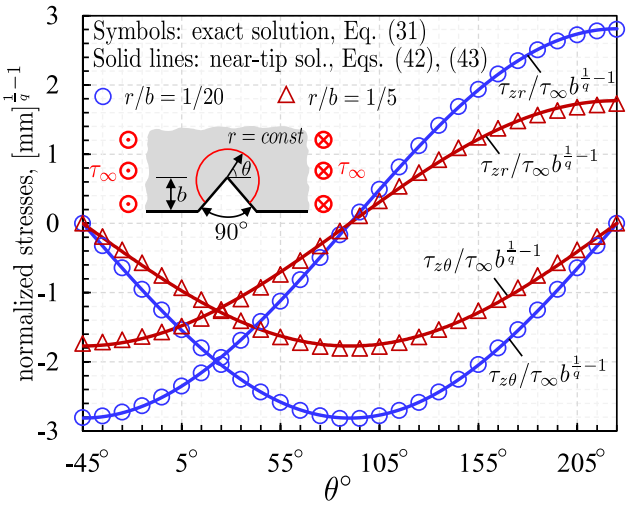

Fig. 8. Normalized stress distributions $\tau_{z\theta}/\tau_\infty b^{\frac{1}{q}-1}$ and $\tau_{zr}/\tau_\infty b^{\frac{1}{q}-1}$ along circular paths of radii $r = 1/20b$ and $r = 1/5b$ centered at the tip and embracing the notch. The notch opening angle, 2α, is equal to 90° in both cases.

true for quasibrittle media featuring a finite FPZ provided that Irwin's characteristic length, $l_{ch} = G_{IIIc}G/f_s^2$ (Irwin, 1958) with G = shear modulus, G_{IIIc} = mode-III fracture energy, and f_s = shear strength, is smaller than $b/10$ (Bažant and Planas, 1997; Bažant et al., 2021). Of course, for all the other cases one can always use the exact solution, Eq. (16), which captures the transition from the singular field to the remote stress τ_∞ (Fig. 7).

Fig. 8 shows the normalized stresses $\tau_{z\theta}/\tau_\infty b^{\frac{1}{q}-1}$ and $\tau_{zr}/\tau_\infty b^{\frac{1}{q}-1}$ along circular paths of radii $r = 1/20b$ and $r = 1/5b$ centered at the tip and embracing the notch for an opening angle $2\alpha = 90°$. Again, the symbols represent the exact solution calculated numerically by means of Eq. (16) while the solid lines show the stresses calculated using the near-tip solution, Eqs. (23) and (24). It is interesting to note that the near-tip solution provides a very good approximation of the stresses for both the radii.

2.5. Finite V-notch with circular end hole

The mapping for the finite V-notch with a circular end hole can be obtained introducing the following transformation on the V-notch curvilinear coordinates:

$$\xi_v = u_v + iv_v = p(\xi,t) = \frac{i}{2}\left(-i\xi + \sqrt{4t^2-\xi^2}\right) \tag{25}$$

where ξ_v represents the curvilinear coordinates of the conformal map describing a finite V-notch of depth b (see Eq. (12)), and ξ represents the curvilinear coordinates of the finite V-notch of depth b and a final circular end hole of radius a as shown in Fig. 9. By introducing the change of coordinates in Eq. (12), the following expression can be found:

$$Z(\xi) = \frac{A_v \pi \exp\left[i\left(\alpha - \frac{\pi}{2}\right)\right]}{2(\pi-\alpha)}\left[\frac{i}{2}\left(-i\xi + \sqrt{4t^2-\xi^2}\right)\right]^{2-\frac{2\alpha}{\pi}} \chi(\alpha,t,\xi) + ib \tag{26}$$

where:

$$\chi(\alpha,t,\xi) = H[\alpha, p(\xi,t)] = {}_2F_1 \times \left\{\frac{1}{2} - \frac{\alpha}{\pi}, 1 - \frac{\alpha}{\pi}, 2 - \frac{\alpha}{\pi}, \left[\frac{i}{2}\left(-i\xi + \sqrt{4t^2-\xi^2}\right)\right]^2\right\} \tag{27}$$

and t is a parameter depending on the ratio between the notch radius and depth, a/b, while the constant A_v was defined in Eq. (13). Fig. 9 shows how Eq. (26) transforms the upper half-plane into the desired semi-infinite plane weakened by a V-notch with a circular end hole.

Once the conformal mapping of the notch is known, the stresses can be calculated by extracting the real and imaginary parts from the following simple expression:

$$\tau_{zx} - i\tau_{zy} = \psi \frac{d\xi(z)}{dz} = \psi\left(\frac{dZ(\xi)}{d\xi}\right)^{-1} = \tau_\infty g(\xi) \tag{28}$$

where:

$$g(\xi,t) = \frac{2^{\frac{1}{2}-\frac{\alpha}{\pi}}\sqrt{4t^2-\xi^2}\left(\xi + i\sqrt{4t^2-\xi^2}\right)^{\frac{2\alpha}{\pi}}}{\left[-2\left(1+t^2\right) + \xi\left(\xi + i\sqrt{4t^2-\xi^2}\right)\right]^{-\frac{1}{2}+\frac{\alpha}{\pi}}\left[2it^2 + \xi\left(-i\xi + \sqrt{4t^2-\xi^2}\right)\right]} \tag{29}$$

and $\tau_\infty = \lim_{\|\xi\|\to 0}\tau_{zx} - i\tau_{zy}$ is the applied remote stress. Eq. (28) provides the expression of the stresses as a function of curvilinear coordinates in the whole domain. Contour plots of the shear stress components calculated by means of Eq. (28) are shown in Fig. 10a,b.

2.5.1. Maximum shear stress at the notch tip

Owed to the complexity of Eqs. (26) and (28), providing explicit expressions for the stresses as a function of Cartesian coordinates can be particularly cumbersome. However, simple relationships can be easily found to describe the stress fields close to the tip of the notch as it was done in Section 2.4.1 for the finite V-notch. By expanding Eq. (29) in Laurent series around $\xi = 0$, which defines the location of the notch tip, and retaining only the linear terms of the expansion one gets:

$$g(\xi,t) \approx \frac{2}{t^{1-2\alpha/\pi}}\left(1+t^2\right)^{1/2-\alpha/\pi} + i\frac{t^{2\alpha/\pi-2}\left[\pi\left(2+t^2\right)-2\alpha\right]}{\left(1+t^2\right)^{1/2+\alpha/\pi}\pi}\xi \tag{30}$$

which, by setting the condition for the notch tip ($\xi = 0$) and combining it with Eq. (28), gives the expression for the maximum shear stress:

$$\tau_{zx}^{\max} = 2\tau_\infty\left[\frac{\sqrt{1+t^2}}{t}\right]^{1-2\alpha/\pi} \tag{31}$$

This simple expression, presented for the first time in this work, shows that the maximum shear stress depends on the remote stress τ_∞, the notch opening angle 2α, and the notch radius/depth ratio a/b through the parameter t. It is difficult to express the dependence of t on the ratio a/b in closed-form however, a very accurate approximation can be found in Appendix A.

Thanks to Eqs. (31), (A.2), and (A.3), it is possible to calculate the stress concentration factor, $\tau_{zx}^{max}/\tau_\infty$, as a function of the ratio between the notch depth and radius, $\rho = a/b$ for various notch opening angles, 2α, as shown in Fig. 11. As can be noted from the figure, ρ has a significant effect on the maximum stress regardless of the notch opening angle. In particular, a smaller ρ leads to higher stress concentrations with the limit case $\rho \to 0$ leading to a stress singularity. On the other hand, it is interesting to note that the dependence of the stress concentration factor on the notch opening angle is more complex. In the range $\rho \in (0, 0.2]$ the opening angle has a significant effect on the stress concentration, lower 2α leading to higher concentrations. However, for $\rho > 0.2$, the effect of the notch opening angle becomes negligible, with all the curves converging to one master curve regardless of the value of 2α.

2.5.2. Near-tip stress field

After the maximum stress is found, the stress field close to the notch tip can be found using the following conformal map describing an infinite V-notch with an end hole:

$$z = i\left[\frac{1}{2}\left(-i\xi + \sqrt{4a^{2/q}-\xi^2}\right)\right]^q \tag{32}$$

where $q = 2(\pi-\alpha)/\pi$. This transformation is obtained by introducing the transformation defined in Eq. (25) into the conformal map z =

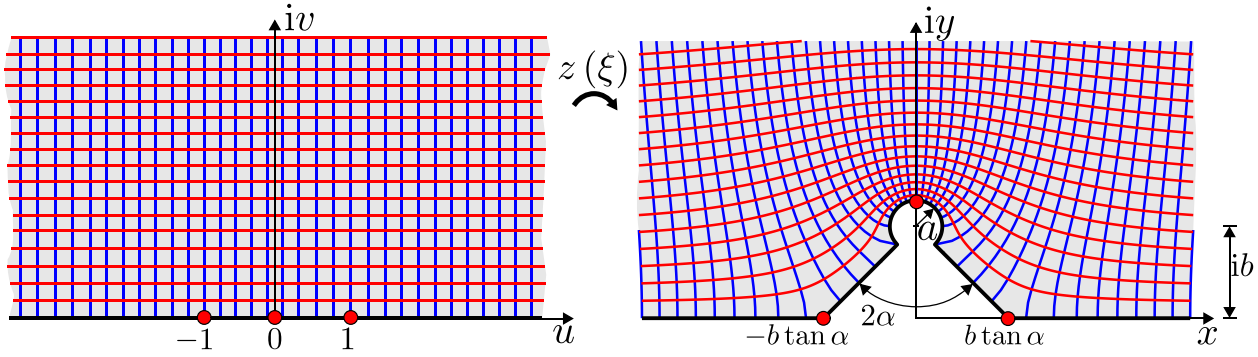

Fig. 9. Schematic representation of the conformal map provided by Eq. (26), transforming the upper half-plane $v \geq 0$, into a semi-infinite domain featuring a finite V-notch with circular end hole of depth b, radius a, and opening 2α.

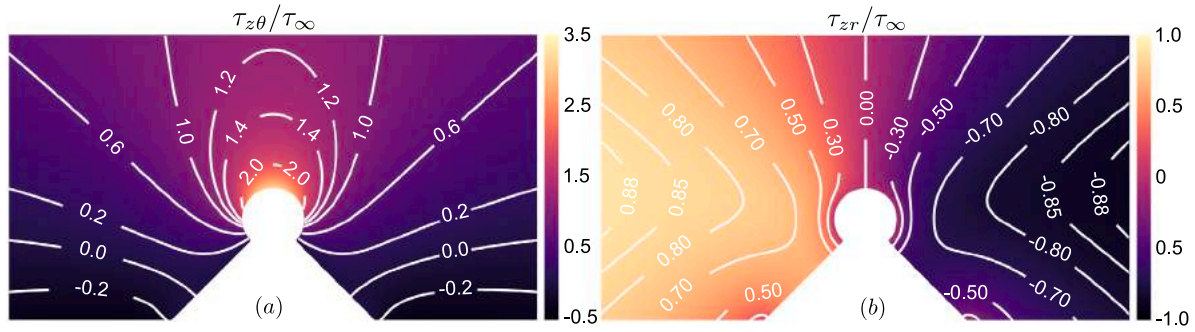

Fig. 10. Normalized stress distribution for a finite V-notch of depth $b = 5$ mm and opening angle $2\alpha = 90°$ with circular end hole of radius $a = 0.3b$ subjected to a remote stress $\lim_{z\to\infty} \tau_{zx} = -\tau_\infty$: (a) $\tau_{z\theta}/\tau_\infty$ and (b) τ_{zr}/τ_∞.

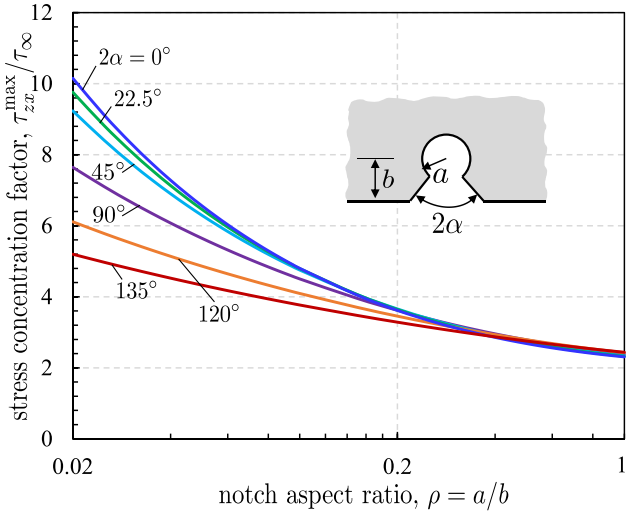

Fig. 11. Stress concentration factor for a finite V-notch with a circular end hole as a function of the ratio between the notch depth and radius, $\rho = a/b$, calculated leveraging Eqs. (31), (A.2), and (A.3).

$i\xi^q$ which describes a deep hyperbolic notch of opening 2α (Neuber, 1958a,b). Since only the stress field close of the tip is of interest and the stress concentration factor is known from the previous calculations, the effects of the finiteness of the V-notch portion can be neglected. This makes it possible to express the curvilinear coordinate ξ as a function of z:

$$\xi = i\left[-a^{2/q}(-iz)^{-1/q} + (-iz)^{1/q}\right] \tag{33}$$

Now, the stresses can be easily calculated in polar coordinates as follows:

$$\begin{aligned}\tau_{zr} - i\tau_{z\theta} &= \psi \exp(i\theta)\frac{\mathrm{d}\xi(z)}{\mathrm{d}z} \\ &= i\frac{\psi}{q}\exp(i\theta)\left[a^{2/q}(-i)^{-1/q}z^{-1-1/q} + (-i)^{1/q}z^{-1+1/q}\right]\end{aligned} \tag{34}$$

which, after a few algebraic manipulations and extracting the real and imaginary parts can be written as:

$$\tau_{zr} = \frac{\psi r^{1/q-1}}{q}\left[\left(\frac{a}{r}\right)^{2/q}\sin\left(\theta - \frac{\pi}{2}\right) - \sin\left(\theta - \frac{\pi}{2}\right)\right] \tag{35}$$

$$\tau_{z\theta} = \frac{\psi r^{1/q-1}}{q}\left[\left(\frac{a}{r}\right)^{2/q}\cos\left(\theta - \frac{\pi}{2}\right) + \cos\left(\theta - \frac{\pi}{2}\right)\right] \tag{36}$$

By setting $\theta = \pi/2$ and $r = a$ it is possible to find the relation between the constant ψ and the maximum shear stress:

$$\tau_{z\theta}^{max} = \frac{2\psi a^{1-1/q}}{q} \tag{37}$$

Finally, the stress equations can be rewritten as a function of the maximum stress:

$$\tau_{zr} = \frac{\tau_{z\theta}^{max}}{2}\left(\frac{r}{a}\right)^{1/q-1}\left[\left(\frac{a}{r}\right)^{2/q}\sin\left(\theta - \frac{\pi}{2}\right) - \sin\left(\theta - \frac{\pi}{2}\right)\right] \tag{38}$$

$$\tau_{z\theta} = \frac{\tau_{z\theta}^{max}}{2}\left(\frac{r}{a}\right)^{1/q-1}\left[\left(\frac{a}{r}\right)^{2/q}\cos\left(\theta - \frac{\pi}{2}\right) + \cos\left(\theta - \frac{\pi}{2}\right)\right] \tag{39}$$

where $\tau_{z\theta}^{max}$ was derived from the full-field stress distribution, Eq. (28), in the previous sections and can be calculated leveraging Eqs. (A.2) and (A.3).

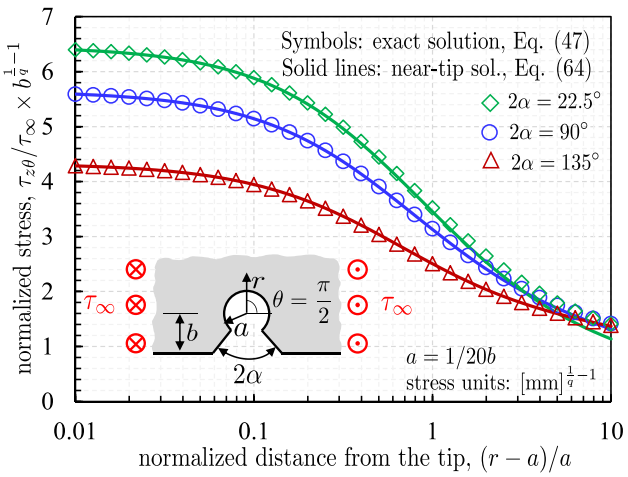

Fig. 12. Normalized stress, $\tau_{z\theta}/\tau_\infty b^{\frac{1}{q}-1}$, as a function of the normalized distance from the notch tip along the bisector, $(r-a)/a$ for $a = 1/20b$.

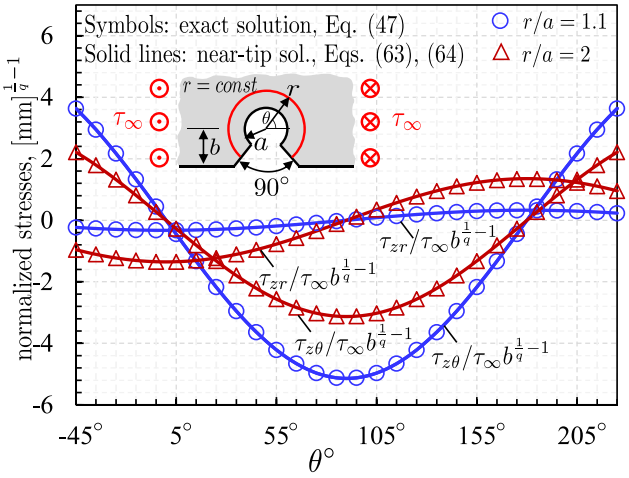

Fig. 13. Normalized stresses, $\tau_{z\theta}/\tau_\infty b^{\frac{1}{q}-1}$ and $\tau_{zr}/\tau_\infty b^{\frac{1}{q}-1}$, along circumferential paths embracing a V-notch with a circular end hole of radius $a = 1/20b$.

It is worth noting that Eqs. (38) and (39) agree with the equations proposed by Zappalorto and Lazzarin (2011) for the analysis of deep V-notches with circular end holes. However, the solution presented for the first time in this work is more comprehensive since it can be applied to both finite and deep notches and it accounts for the effects of the depth of the notch and the radius of the end hole. The latter condition is necessary to be able to calculate the maximum stress $\tau_{z\theta}^{max}$ without relying on numerical approaches such as the Finite Element Method (FEM).

The stress distributions calculated by means of the exact and near-tip solutions are shown in Figs. 12 and 13. Fig. 12 shows the normalized stress, $\|\tau_{z\theta}\|/\tau_\infty b^{\frac{1}{q}-1}$, as a function of the normalized distance from the notch tip along the bisector, $(r-a)/a$ in semi-logarithmic scale for various notch opening angles and $a = 1/20b$. The symbols represent the exact solution calculated numerically by means of Eq. (28) while the solid lines show the stresses calculated using the near-tip solution, Eq. (39). As can be noted, the near-tip solution, Eq. (39), provides a remarkably good approximation of the exact solution.

Fig. 13 shows the normalized stresses $\tau_{z\theta}/\tau_\infty b^{\frac{1}{q}-1}$ and $\tau_{zr}/\tau_\infty b^{\frac{1}{q}-1}$ along circular paths of radii $r = 1.1a$ and $r = 2a$ embracing the notch for an opening angle $2\alpha = 90°$. Again, the symbols represent the exact solution calculated numerically by means of Eq. (28) while the solid lines show the stresses calculated using the near-tip solution, Eqs. (38) and (39). It is interesting to note that the near-tip solution provides a very good approximation of the stresses for both the radii.

3. V-notch with circular region of a different material embracing the tip

The previous sections analyzed the displacement and stress distributions for the case of a V-notch and a V-notch with a circular end hole. As explained in Section 2.3, these distributions are required to find the solution for a V-notch featuring a circular region of a different material embracing the tip (Fig. 3). Hence, after obtaining the foregoing novel results, the next step is to characterize the constants A, B, and C utilized in Eqs. (9)(e) and (9)(f) to calculate the displacements in regions Ω^A and Ω^B. This can be accomplished by imposing the equilibrium and compatibility conditions on the interface, Eqs. (10)(a) and (10)(b), and the remote condition $\lim_{\xi\to\infty}\tau_{zx} = \tau_\infty$. Towards this goal, it is convenient to note that $v = 0$ on the interface Ω^{A-B} so that the following relation between the coordinates ξ_v and ξ holds:

$$u_v + iv_v = \frac{u}{2} + \frac{i}{2}\sqrt{4t^2 - u} \tag{40}$$

which means that at the interface, where $r = a$, the following simple relation between the curvilinear coordinates applies: $u = 2u_v$. Substituting this result into Eqs. (9)(e) and (9)(f) and performing a few algebraic manipulations gives the following system of equations:

$$\begin{cases} G_A C = G_B A & \text{(a)} \\ C = A + 2B & \text{(b)} \end{cases} \tag{41}$$

which leads to $C = 2B/\left(1 - G_A/G_B\right)$ and $A = G_A/G_B\left[2B/\left(1 - G_A/G_B\right)\right]$. To determine the value of the constant B, one can impose the remote condition:

$$\tau_\infty = \lim_{\xi\to\infty}\frac{G_B}{h}\frac{\partial w_B}{\partial u} = G_B(A + B) \tag{42}$$

Then, after combining Eqs. (41)(a), (41)(b), and (42) it is finally possible to get the following expressions:

$$A = \frac{2G_A\tau_\infty}{G_B^2\left(1 + G_A/G_B\right)} \tag{43}$$

$$B = \frac{\tau_\infty}{G_B}\frac{\left(1 - G_A/G_B\right)}{\left(1 + G_A/G_B\right)} \tag{44}$$

$$C = \frac{2\tau_\infty}{G_B\left(1 + G_A/G_B\right)} \tag{45}$$

Substituting into Eqs. (10)(a) and (10)(b) the displacement can be calculated as follows:

$$w = \begin{cases} \dfrac{2\tau_\infty}{G_B\left(1 + G_A/G_B\right)}u_v & \text{for } \xi_v \in \Omega^A \quad \text{(a)} \\ \dfrac{2G_A\tau_\infty}{G_B^2\left(1 + G_A/G_B\right)}u_v(u, v) + \dfrac{\tau_\infty}{G_B}\dfrac{\left(1 - G_A/G_B\right)}{\left(1 + G_A/G_B\right)}u & \text{for } \xi \in \Omega^B \quad \text{(b)} \end{cases} \tag{46}$$

showing that the displacement depends on the domain geometry through the curvilinear coordinates u_v, u, and v, the remote stress τ_∞, and the shear moduli G_A and G_B.

After deriving the equation for the displacement, the stresses in region Ω^A can be calculated using the following relation:

$$\begin{aligned} \tau_{zx} - i\tau_{zy} &= G_A C\frac{\mathrm{d}\xi_v(z)}{\mathrm{d}z} = G_A C\left(\frac{\mathrm{d}Z\left(\xi_v\right)}{\mathrm{d}\xi_v}\right)^{-1} \\ &= \frac{2\tau_\infty G_A/G_B}{\left(1 + G_A/G_B\right)}\frac{\left(\xi_v^2 - 1\right)^{1/2-\alpha/\pi}}{\xi_v^{1-2\alpha/\pi}} \end{aligned} \tag{47}$$

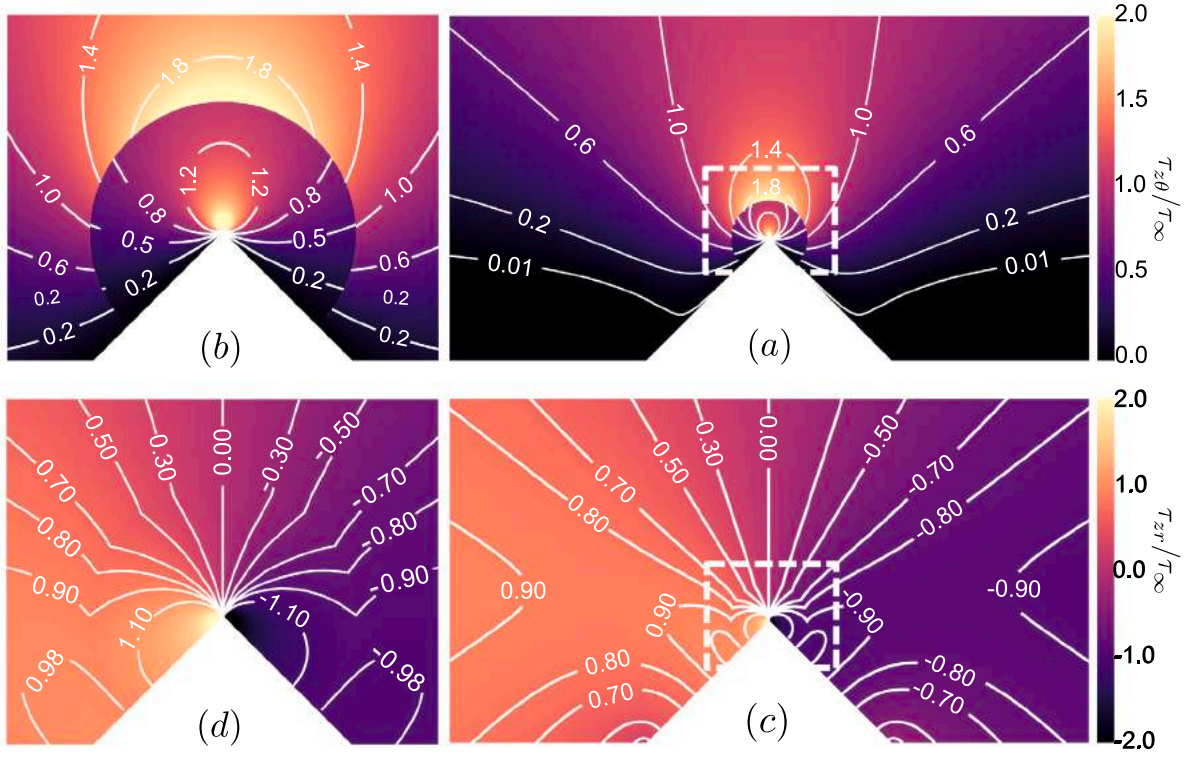

Fig. 14. Normalized stress distribution for a finite V-notch of depth $b = 5$ mm and opening angle $2\alpha = 90°$ with circular region made of different material of radius $a = 0.3b$ embracing the tip. The notch is subjected to a remote stress $\lim_{z\to\infty} \tau_{zx} = -\tau_\infty$. The material inside the circular region Ω^A features a shear modulus $G_A = 1500$ MPa while the outer region, Ω^B, has a shear modulus $G_B = 3000$ MPa: (a) $\tau_{z\theta}/\tau_\infty$, (b) magnified view, (c) τ_{zr}/τ_∞, and (d) magnified view. Note the discontinuity on $\tau_{z\theta}/\tau_\infty$ on the interface between Ω^A and Ω^B while τ_{zr}/τ_∞ is perfectly continuous for equilibrium.

By extracting the real and imaginary parts of the equation, the stresses can be written as follows:

$$\tau_{zx}\left(u_v, v_v\right) = \frac{2\tau_\infty G_A/G_B}{\left(1+G_A/G_B\right)} \frac{\left[\left(u_v^2 - v_v^2 - 1\right)^2 + 4u_v^2 v_v^2\right]^{1/4-\alpha/2\pi}}{\left(u_v^2+v_v^2\right)^{1/2-\alpha/\pi}} \cos\eta \tag{48}$$

$$\tau_{zy}\left(u_v, v_v\right) = \frac{2\tau_\infty G_A/G_B}{\left(1+G_A/G_B\right)} \frac{\left[\left(u_v^2 - v_v^2 - 1\right)^2 + 4u_v^2 v_v^2\right]^{1/4-\alpha/2\pi}}{\left(u_v^2+v_v^2\right)^{1/2-\alpha/\pi}} \sin\eta \tag{49}$$

where $\eta = (\alpha/\pi - 1/2)\arg\left(u_v^2 - v_v^2 - 1 + 2iu_v v_v\right) + (1-2\alpha/\pi)\arg\left(u_v + iv_v\right)$. It is worth mentioning that Eqs. (48) and (49) differ from the expressions for the homogeneous case, Eqs. (16) and (17), only for the factor $2G_A/[G_B(1+G_A/G_B)]$. It is interesting to note that for $G_A/G_B \to 1$, Eqs. (48) and (49) tend to the homogeneous case. On the other hand, for the case in which region Ω^A is significantly stiffer than Ω^B, $G_A/G_B \to \infty$, the multiplying factor tends to 2. This means that, in such scenario, the stresses in Ω^A tend to be two times larger than the homogeneous case for the same remote stress τ_∞. As expected, the case in which region Ω^A is significantly more compliant than Ω^B, $G_A/G_B \to 0$, leads to negligible stresses.

For region Ω^B, the stresses can be calculated starting from the following equation:

$$\begin{aligned}\tau_{zx} - i\tau_{zy} &= G_B\left[A\frac{\mathrm{d}\xi_v(z)}{\mathrm{d}z} + B\frac{\mathrm{d}\xi(z)}{\mathrm{d}z}\right] \\ &= G_B\left[A\left(\frac{\mathrm{d}Z(\xi_v)}{\mathrm{d}\xi_v}\right)^{-1} + B\left(\frac{\mathrm{d}Z(\xi)}{\mathrm{d}\xi}\right)^{-1}\right]\end{aligned} \tag{50}$$

which, after inserting Eqs. (43)–(45), gives:

$$\tau_{zx} - i\tau_{zy} = \frac{2\tau_\infty G_A/G_B}{1+G_A/G_B} f\left(\xi_v\right) + \tau_\infty \frac{1-G_A/G_B}{1+G_A/G_B} g\left(\xi, t\right) \tag{51}$$

where:

$$f\left(\xi_v\right) = \frac{\left(\xi_v^2-1\right)^{1/2-\alpha/\pi}}{\xi_v^{1-2\alpha/\pi}} \tag{52}$$

and $g(\xi, t)$ was defined in Eq. (29). By taking the real and imaginary parts of the equation, it is possible to extract the stress components as a function of the curvilinear coordinates ξ_v and ξ. In regard to the stresses, it is interesting to note that for $G_A/G_B \to 0$ the stresses in Eq. (51) tend to the ones of the homogeneous case of the V-notch with a circular end hole, Eq. (28). Of course, this is expected since in this case region Ω^A acts as an empty space. Furthermore, $G_A/G_B \to 1$ gives the homogeneous case of a finite V-notch, Eq. (15). Finally, for $G_A/G_B \to \infty$ the stresses depend on the contribution of both the domains Ω^A and Ω^B: $\tau_{zx} - i\tau_{zy} = \tau_\infty\left[2f\left(\xi_v\right) - g\left(\xi\right)\right]$.

Contour plots of the shear stresses calculated by means of Eqs. (47) and (51) for $b = 5$ mm, $a = 0.3b$, $2\alpha = 90°$, and $G_A/G_B = 1/2$ are shown in Fig. 14(a–d). As can be noted, the difference in material properties leads to a significant discontinuity in the tangential component of the stress Fig. 14(a,b). On the other hand, the radial component of the stress is continuous throughout the entire domain for equilibrium as shown by Fig. 14(c, d).

3.1. Near-tip stress field

The stress field near the tip of the V-notch can be calculated leveraging the equation for the near-tip stress field of the homogeneous case, Eq. (18). Noting that for the multi-material case the stresses in region Ω^A differ from the homogeneous case only for a multiplying factor, one can easily obtain the following expression:

$$\tau_{zx} - i\tau_{zy} = \frac{2\tau_\infty G_A/G_B}{\left(1+G_A/G_B\right)} \exp\left[\frac{\pi(q-1)}{2q}i\right]\left(\frac{A_v}{q}\right)^{1/q-1} z^{1/q-1} \tag{53}$$

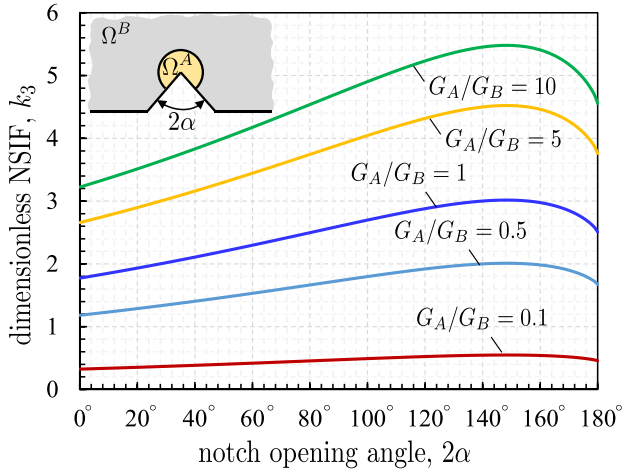

Fig. 15. Evolution of the dimensionless Notch Stress Intensity Factor (NSIF), Eq. (56), as a function of the notch opening angle for various ratios G_A/G_B. Note that, for a given opening angle, stiffer materials in region Ω^A lead to higher dimensionless NSIFs.

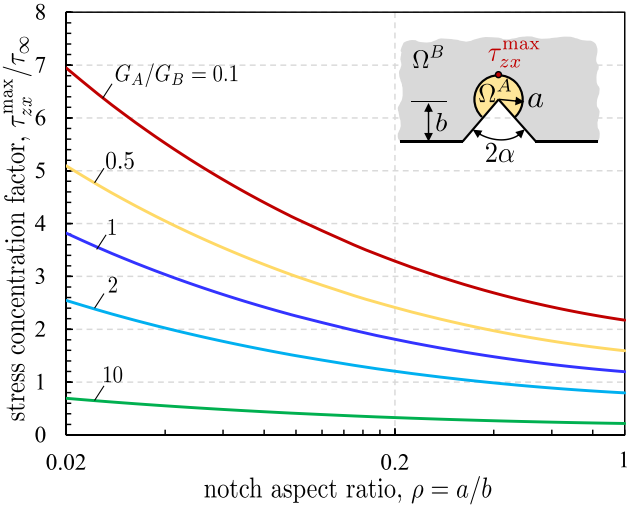

Fig. 16. Stress concentration factor in region Ω^B calculated by means of Eq. (57) as a function of the notch aspect ratio, $\rho = a/b$, for various sets of elastic properties. The notch opening angle is $2\alpha = 90°$. Note that, for a given ρ, lower G_A/G_B ratios lead to higher concentration factors.

Based on the foregoing equation, the NSIF (Gross and Mendelson, 1972) can be easily determined leveraging its definition:

$$K_3 = \sqrt{2\pi}\lim_{y\to 0}\tau_{zx}y^{1-1/q} = \frac{2\tau_\infty G_A/G_B}{(1+G_A/G_B)}\sqrt{2\pi}\left(\frac{A_v}{q}\right)^{1-1/q} = \frac{2\tau_\infty G_A/G_B}{(1+G_A/G_B)} \times \sqrt{2\pi}\left[\frac{b\sqrt{\pi}/\cos\alpha}{q\Gamma(1-\alpha/\pi)\,\Gamma(1/2+\alpha/\pi)}\right]^{1-1/q} \tag{54}$$

or, in a more compact form:

$$K_3 = \tau_\infty b^{1-1/q}k_3\left(\alpha, G_A/G_B\right) \tag{55}$$

where:

$$k_3\left(\alpha, G_A/G_B\right) = \frac{2\sqrt{2\pi}G_A/G_B}{(1+G_A/G_B)}\left[\frac{\sqrt{\pi}/\cos\alpha}{q\Gamma(1-\alpha/\pi)\,\Gamma(1/2+\alpha/\pi)}\right]^{1-1/q} \tag{56}$$

is a dimensionless function that, different from the homogeneous case, depends not only on the opening angle 2α but also the ratio between the shear moduli G_A/G_B. It is interesting to note that the dependence of K_3 on the notch depth, b, features the same exponent $1-1/q$ as the homogeneous case which only depends on the notch opening angle.

Fig. 15 shows the dimensionless Notch Stress Intensity Factor $k_3\left(\alpha, G_A/G_B\right)$ as a function of the notch opening angle for various sets of elastic properties. As can be noted, the elastic properties have a significant effect on the NSIF, regardless of the opening angle. In particular, the figure shows that increasing the ratio G_A/G_B leads to higher values of the NSIF. This result is particularly interesting since it means that it is possible to reduce the NSIF of the notch by finely controlling the material introduced in the circular region embracing the tip.

After calculating the NSIF leveraging Eqs. (55) and (56), the Cartesian and polar stress distributions can be calculated leveraging Eqs. (21), (22) and (23), (24) respectively.

3.2. Maximum stress in Ω^B

In addition to the NSIF, it is important to investigate how the maximum stress in Ω^B is affected by the material and geometrical configurations. Towards this goal, it is useful to note that $v = u = u_v = 0$ at the point of maximum stress. Considering Eq. (25), this means that $v_v = t$ in the location of maximum stress. Inserting this result into Eq. (51) and extracting the real part of the equation leads to the following expression for the maximum stress:

$$\tau_{zx}^{max} = \frac{2\tau_\infty}{1+G_A/G_B}\left(\frac{\sqrt{1+t^2}}{t}\right)^{1-\frac{2\alpha}{\pi}} \tag{57}$$

It is interesting to note that the foregoing equation differs from the homogeneous case, Eq. (31), only for the multiplying factor $1/(1+G_A/G_B)$. As expected, when $G_A/G_B \to 0$, the stress concentration tends to the homogeneous case of V-notch with a circular end hole. For the case in which the material in Ω^A is very stiff compared to the one in Ω^B, $G_A/G_B \to \infty$, the maximum stress in Ω^B becomes negligible.

It is noteworthy that the maximum stress in Ω^B decreases for increasing values of G_A/G_B which is an opposite trend compared to the evolution of the NSIF. This means that particular care must be devoted to the selection of the combination of materials in Ω^A and Ω^B. Selecting a very soft material in Ω^A does reduce the NSIF but it does so at the expenses of the stress concentration in Ω^B, which increases. Ultimately the best combination is the one that leads to the maximum structural capacity by striking the right balance between NSIF reduction and stress concentration increase.

A summary of these observations is provided in Fig. 16 which shows the evolution of the stress concentration factor as a function of $\rho = a/b$ for various G_A/G_B and an opening angle of 90°.

4. V-notch with two circular regions of a different material embracing the tip

The general theoretical framework introduced for the first time in the present study can be used for any number of circular domains embracing the notch tip.

Let us consider three conformal mappings $z = z\left(\xi_v\right)$, $z = z\left(\xi_1\right)$, and $z = z\left(\xi_2\right)$ with $\xi_v = u_v + iv_v$, $\xi_1 = u_1 + iv_1$, and $\xi_2 = u_2 + iv_2$. The three maps are defined so that the condition $v_v = v_{v,0}$ describes $\partial\Omega^A_{n,0} \cup \partial\Omega^B_{n,0} \cup \partial\Omega^C_{n,0}$, the condition $v_1 = v_{1,0}$ describes $\partial\Omega^B_{n,0} \cup \partial\Omega^C_{n,0} \cup \partial\Omega^{A-B}$ while $v_2 = v_{2,0}$ describes $\partial\Omega^C_{n,0} \cup \partial\Omega^{B-C}$ (see Fig. 17). This means that ξ_v represents the curvilinear coordinates of the map for a finite V-notch of opening angle 2α and depth b as described in Eq. (12) while ξ_1 and ξ_2 describe the curvilinear coordinates for a finite V-notch with circular end hole of radii a_1 and a_2 respectively as described by Eq. (26).

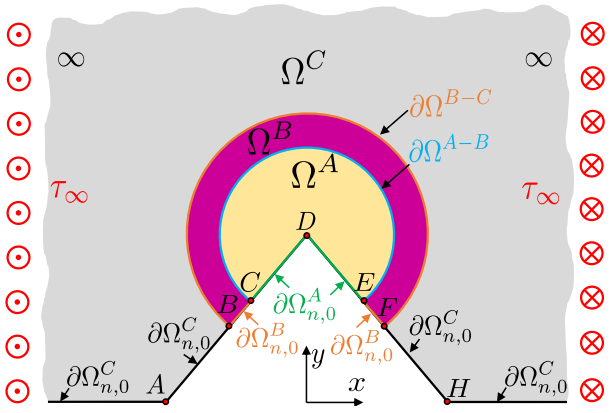

Fig. 17. Example of semi-infinite domain $\Omega = \Omega^A \cup \Omega^B \cup \Omega^C$ with a finite notch featuring two regions of different materials surrounding the tip. The $\tau_{zn} = 0$ condition is applied to $\Omega^A_{n,0}$, $\Omega^B_{n,0}$ and $\Omega^C_{n,0}$ for regions A, B, and C. Ω^{A-B} represents the interface between regions A and B while Ω^{B-C} represents the interface between regions B and C.

The relation between the three curvilinear variables is as follows:

$$\xi_v = \frac{i}{2}\left(-i\xi_1 + \sqrt{4t_1^2 - \xi_1^2}\right) = \frac{i}{2}\left(-i\xi_2 + \sqrt{4t_2^2 - \xi_2^2}\right) \tag{58}$$

where t_1 and t_2 are parameters that depend on the ratio between the radius of the circular regions and the depth of the notch. They can both be calculated leveraging Eqs. (A.2) and (A.3).

Similar to what was done in Section 2, one can impose the equilibrium equations in each region of the multimaterial domain along with the related compatibility and equilibrium conditions on the interfaces. This leads to the following system of equations:

$$\begin{cases}
\dfrac{\partial^2 w_A}{\partial u_v^2} + \dfrac{\partial^2 w_A}{\partial v_v^2} = 0, & \text{for } \xi_v \in (-\infty,\infty)\times\left[v_{v,0},\infty\right) \quad \text{(a)}\\
\dfrac{\partial w_A}{\partial v_v} = 0, & \text{for } v_v = v_{v,0} \quad \text{(b)}\\
\dfrac{\partial^2 w_B}{\partial u^2} + \dfrac{\partial^2 w_B}{\partial v^2} = 0, & \text{for } \xi \in (-\infty,\infty)\times\left[v_{1,0},\infty\right) \quad \text{(c)}\\
\dfrac{\partial w_B}{\partial v} = 0, & \text{for } v = v_{1,0} \quad \text{(d)}\\
\dfrac{\partial^2 w_C}{\partial u^2} + \dfrac{\partial^2 w_C}{\partial v^2} = 0, & \text{for } \xi \in (-\infty,\infty)\times\left[v_{2,0},\infty\right) \quad \text{(e)}\\
\dfrac{\partial w_C}{\partial v} = 0, & \text{for } v = v_{2,0} \quad \text{(f)}\\
G_A\dfrac{\partial \omega_A}{\partial v_1} = G_B\dfrac{\partial w_B}{\partial v_1}, & \text{for } \xi \in \partial\Omega^{A-B} \quad \text{(g)}\\
G_B\dfrac{\partial \omega_B}{\partial v_2} = G_C\dfrac{\partial w_C}{\partial v_2}, & \text{for } \xi \in \partial\Omega^{B-C} \quad \text{(h)}\\
\omega_A = w_B, & \text{for } \xi \in \partial\Omega^{A-B} \quad \text{(i)}\\
\omega_B = w_C, & \text{for } \xi \in \partial\Omega^{B-C} \quad \text{(j)}
\end{cases} \tag{59}$$

where $\omega_A\left(u_1, v_1\right) = w_A\left[u_v\left(u_1, v_1\right), v_v\left(u_1, v_1\right)\right]$ represents the displacement in region Ω^A written as a function of the curvilinear coordinates u_1, v_1. On a similar note, $\omega_B\left(u_2, v_2\right) = w_B\left[u_1\left(u_2, v_2\right), v_1\left(u_2, v_2\right)\right]$ represents the displacement in region Ω^B written as a function of the curvilinear coordinates u_2, v_2. The shear moduli in regions Ω^A, Ω^B, and Ω^C are G_A, G_B, and G_C. In the foregoing system, Eqs (59)(a), (59)(c), and (59)(e) represent the equilibrium equations in Ω^A, Ω^B, and Ω^C. Eqs. (59)(b), (59)(d), and (59)(f) are the equilibrium conditions on the stress-free boundary. Eqs. (59)(g) and (59)(h) describe the equilibrium condition on the interfaces $\partial\Omega^{A-B}$ and $\partial\Omega^{B-C}$ respectively. Finally, Eqs. (59)(i) and (59)(j) represent the compatibility condition on the interfaces.

Following the same theoretical framework described in Sections 2 and 3, the solution of Eqs. (59)(a)–(59)(j) can be found leveraging the following displacement function:

$$w = \begin{cases}
w_A\left(u_v, v_v\right) = Cu_v, & \text{for } \xi_v \in \Omega^A \quad \text{(a)}\\
w_B\left(u_1, v_1\right) = Au_v\left(u_1, v_1\right) + Bu_1, & \text{for } \xi_1 \in \Omega^B \quad \text{(b)}\\
w_C\left(u_2, v_2\right) = Mu_1\left(u_2, v_2\right) + Gu_2, & \text{for } \xi_2 \in \Omega^C \quad \text{(c)}
\end{cases} \tag{60}$$

where A, B, C, M, G are real constants to be found by imposing equilibrium and compatibility conditions on the interfaces and the remote stress condition.

At this point, it is useful to point out that, as discussed in the foregoing sections, $u_1 = 2u_v$ along the interface Ω^{A-B}. Along the interface Ω^{B-C}, on the other hand, $v_2 = 0$. Combining this result with Eq. (58) and extracting only the real part of the equation provides the following simple relation between the curvilinear coordinates u_1 and u_2:

$$u_1 = \frac{1}{2}\left[1 + \left(\frac{t_1}{t_2}\right)^2\right] u_2 \tag{61}$$

Substituting this expression into Eqs. (59)(a)–(59)(j) and imposing the remote stress condition:

$$\tau_\infty = \lim_{\xi\to\infty} \frac{G_C}{h}\frac{\partial w_C}{\partial u} = G_C\left(M + G\right) \tag{62}$$

one obtains the following system of equations:

$$\begin{cases}
C = A + 2B & \text{(a)}\\
A + \dfrac{B}{2}\left[1 + \left(\dfrac{t_1}{t_2}\right)^2\right] = \dfrac{M}{2}\left[1 + \left(\dfrac{t_1}{t_2}\right)^2\right] + 2G & \text{(b)}\\
G_A C = G_B A & \text{(c)}\\
G_B\left\{A + B\left[1 - \left(\dfrac{t_1}{t_2}\right)^2\right]\right\} = G_C\left\{M\left[1 - \left(\dfrac{t_1}{t_2}\right)^2\right]\right\} & \text{(d)}\\
\tau_\infty = G_C\left(M + G\right) & \text{(e)}
\end{cases} \tag{63}$$

After a few algebraic manipulations, the system allows the calculation of the desired constants:

$$A = \frac{4\zeta_{AC}t_2^2\tau_\infty}{\left(\zeta_{AC} - \zeta_{BC}\right)\left(\zeta_{BC} - 1\right)t_1^2 + \left(\zeta_{AC} + \zeta_{BC}\right)\left(\zeta_{BC} + 1\right)t_2^2} \tag{64}$$

$$B = \frac{2\left(\zeta_{BC} - \zeta_{AC}\right)t_2^2\tau_\infty}{\left(\zeta_{AC} - \zeta_{BC}\right)\left(\zeta_{BC} - 1\right)t_1^2 + \left(\zeta_{AC} + \zeta_{BC}\right)\left(\zeta_{BC} + 1\right)t_2^2} \tag{65}$$

$$C = \frac{4\zeta_{BC}t_2^2\tau_\infty}{G_C\left[\left(\zeta_{AC} - \zeta_{BC}\right)\left(\zeta_{BC} - 1\right)t_1^2 + \left(\zeta_{AC} + \zeta_{BC}\right)\left(\zeta_{BC} + 1\right)t_2^2\right]} \tag{66}$$

$$G = \frac{\left[\left(\zeta_{BC} - \zeta_{AC}\right)\left(\zeta_{BC} - 1\right)t_1^4 - 2\zeta_{AC}\left(\zeta_{BC} + 1\right)t_1^2t_2^2 - \left(\zeta_{AC} + \zeta_{BC}\right)\left(\zeta_{BC} - 1\right)t_2^4\right]\tau_\infty}{G_C\left[\left(\zeta_{BC} - \zeta_{AC}\right)\left(\zeta_{BC} - 1\right)t_1^4 - 2\left(\zeta_{BC}^2 + \zeta_{AC}\right)t_1^2t_2^2 + \left(\zeta_{AC} + \zeta_{BC}\right)\left(\zeta_{BC} + 1\right)t_2^4\right]} \tag{67}$$

$$M = \frac{2\zeta_{BC}t_2^2\tau_\infty\left[\left(\zeta_{AC} - \zeta_{BC}\right)t_1^2 + \left(\zeta_{AC} + \zeta_{BC}\right)t_2^2\right]}{G_C\left[\left(\zeta_{BC} - \zeta_{AC}\right)\left(\zeta_{BC} - 1\right)t_1^4 - 2\left(\zeta_{BC}^2 + \zeta_{AC}\right)t_1^2t_2^2 + \left(\zeta_{AC} + \zeta_{BC}\right)\left(\zeta_{BC} + 1\right)t_2^4\right]} \tag{68}$$

where $\zeta_{AC} = G_A/G_C$ and $\zeta_{BC} = G_B/G_C$. Substituting the foregoing equations into the displacement equations, Eqs. (60)(a)–(60)(c), it is possible to fully characterize the displacement field except for rigid body motions. The final equations are not shown for conciseness. As can be noted from Eqs. (64)–(68), the displacement constants depend on the ratios between the radii of the circular regions and the notch depth through the parameters t_1 and t_2, the elastic moduli of the various regions through the dimensionless parameters ζ_{AC} and ζ_{BC}, and the remote stress τ_∞. On the other hand, the effect of the notch opening angle, 2α on the displacement is automatically included by having written w as a function of the curvilinear coordinates ξ_v, ξ_1, and ξ_2 which properly describe the border of the notch.

After deriving the equations for the displacement, the stresses in region Ω^A can be calculated using the following relation (see Eq. (7)):

$$\tau_{zx} - i\tau_{zy} = G_A C\frac{\mathrm{d}\xi_v(z)}{\mathrm{d}z} = G_A C\frac{\left(\xi_v^2 - 1\right)^{1/2-\alpha/\pi}}{\xi_v^{1-2\alpha/\pi}} \tag{69}$$

where C is given by Eq. (66). By extracting the real and imaginary parts of the equation, the stresses can be written as follows:

$$\tau_{zx}\left(u_v,v_v\right)=G_A C\frac{\left[\left(u_v^2-v_v^2-1\right)^2+4u_v^2v_v^2\right]^{1/4-\alpha/2\pi}}{\left(u_v^2+v_v^2\right)^{1/2-\alpha/\pi}}\cos\eta \tag{70}$$

$$\tau_{zy}\left(u_v,v_v\right)=G_A C\frac{\left[\left(u_v^2-v_v^2-1\right)^2+4u_v^2v_v^2\right]^{1/4-\alpha/2\pi}}{\left(u_v^2+v_v^2\right)^{1/2-\alpha/\pi}}\sin\eta \tag{71}$$

where $\eta=(\alpha/\pi-1/2)\arg\left(u_v^2-v_v^2-1+2iu_vv_v\right)+(1-2\alpha/\pi)\arg\left(u_v+iv_v\right)$.

For region Ω^B, the stresses can be calculated starting from the following equation:

$$\begin{aligned}\tau_{zx}-i\tau_{zy}&=G_B\left[A\frac{\mathrm{d}\xi_v(z)}{\mathrm{d}z}+B\frac{\mathrm{d}\xi_1(z)}{\mathrm{d}z}\right]\\&=G_B\left[A\left(\frac{\mathrm{d}Z\left(\xi_v\right)}{\mathrm{d}\xi_v}\right)^{-1}+B\left(\frac{\mathrm{d}Z\left(\xi_1\right)}{\mathrm{d}\xi_1}\right)^{-1}\right]\end{aligned} \tag{72}$$

which can be rewritten in a more compact form as follows:

$$\tau_{zx}-i\tau_{zy}=AG_Bf\left(\xi_v\right)+BG_Bg\left(\xi_1,t_1\right) \tag{73}$$

where A and B can be calculated by means of Eqs. (64) and (65) and $g\left(\xi_1,t_1\right)$ and $f\left(\xi_v\right)$ were defined in Eqs. (29) and (52) respectively. By taking the real and imaginary parts of the equation, it is possible to extract the stress components as a function of the curvilinear coordinates ξ_v and ξ_1.

The stresses in region Ω^C can be calculated in a similar way by starting from the following equation:

$$\begin{aligned}\tau_{zx}-i\tau_{zy}&=G_C\left[M\frac{\mathrm{d}\xi_1(z)}{\mathrm{d}z}+G\frac{\mathrm{d}\xi_2(z)}{\mathrm{d}z}\right]\\&=G_C\left[M\left(\frac{\mathrm{d}Z\left(\xi_1\right)}{\mathrm{d}\xi_1}\right)^{-1}+G\left(\frac{\mathrm{d}Z\left(\xi_2\right)}{\mathrm{d}\xi_2}\right)^{-1}\right]\end{aligned} \tag{74}$$

This equation can be rewritten as follows:

$$\tau_{zx}-i\tau_{zy}=MG_Cg\left(\xi_1,t_1\right)+GG_Cg\left(\xi_2,t_2\right) \tag{75}$$

where the constants G and M are computed via Eqs. (67) and (68) respectively. By taking the real and imaginary parts of the equation, it is possible to extract the stress components as a function of the curvilinear coordinates ξ_1 and ξ_2.

Contour plots of the shear stresses calculated by means of Eqs. (70), (71), (73), and (75) for $b=5$ mm, $a_1=0.3b$, $a_2=0.4b$, $2\alpha=90°$, $G_A=1500$ MPa, $G_B=3000$ MPa, and $G_C=4500$ MPa are shown in Fig. 18(a–d). As can be noted, the difference in material properties leads to a significant discontinuity in the tangential component of the stress Fig. 18(a,b). On the other hand, the radial component of the stress is continuous throughout the entire domain for equilibrium as shown by Fig. 18(c, d).

4.1. Near-tip stress field

The stress field near the tip of the V-notch can be calculated leveraging the equation for the near-tip stress field of the homogeneous case, Eq. (18). Noting that for the multi-material case the stresses in region Ω^A differ from the homogeneous case only for the multiplying factor C, one can easily obtain the following expression:

$$\tau_{zx}-i\tau_{zy}=\frac{4\zeta_{BC}\zeta_{AC}t_2^2\tau_\infty\exp\left[\frac{\pi(q-1)}{2q}i\right]\left(\frac{A_v}{q}\right)^{1/q-1}}{\left(\zeta_{AC}-\zeta_{BC}\right)\left(\zeta_{BC}-1\right)t_1^2+\left(\zeta_{AC}+\zeta_{BC}\right)\left(\zeta_{BC}+1\right)t_2^2}z^{1/q-1} \tag{76}$$

Based on the foregoing equation, the NSIF (Gross and Mendelson, 1972) can be easily determined leveraging its definition:

$$\begin{aligned}K_3&=\sqrt{2\pi}\lim_{y\to0}\tau_{zx}y^{1-1/q}\\&=\frac{\sqrt{2\pi}4\zeta_{BC}\zeta_{AC}t_2^2\tau_\infty\left(\frac{A_v}{q}\right)^{1/q-1}}{\left(\zeta_{AC}-\zeta_{BC}\right)\left(\zeta_{BC}-1\right)t_1^2+\left(\zeta_{AC}+\zeta_{BC}\right)\left(\zeta_{BC}+1\right)t_2^2}\\&=\frac{4\sqrt{2\pi}\zeta_{BC}\zeta_{AC}t_2^2\tau_\infty\left[\frac{b\sqrt{\pi}/\cos\alpha}{q\Gamma(1-\alpha/\pi)\Gamma(1/2+\alpha/\pi)}\right]^{1-1/q}}{\left(\zeta_{AC}-\zeta_{BC}\right)\left(\zeta_{BC}-1\right)t_1^2+\left(\zeta_{AC}+\zeta_{BC}\right)\left(\zeta_{BC}+1\right)t_2^2}\end{aligned} \tag{77}$$

or, in a more compact form:

$$K_3=\tau_\infty b^{1-1/q}k_3^{(1)}(\alpha)\,k_3^{(2)}\left(a_1/b,a_2/b,\zeta_{AC},\zeta_{BC}\right) \tag{78}$$

where:

$$k_3^{(1)}(\alpha)=\sqrt{2\pi}\left[\frac{\sqrt{\pi}/\cos\alpha}{q\Gamma(1-\alpha/\pi)\,\Gamma(1/2+\alpha/\pi)}\right]^{1-1/q} \tag{79}$$

$$\begin{aligned}&k_3^{(2)}\left(a_1/b,a_2/b,\zeta_{AC},\zeta_{BC}\right)\\&\quad=\frac{4\zeta_{BC}\zeta_{AC}t_2^2}{\left(\zeta_{AC}-\zeta_{BC}\right)\left(\zeta_{BC}-1\right)t_1^2+\left(\zeta_{AC}+\zeta_{BC}\right)\left(\zeta_{BC}+1\right)t_2^2}\end{aligned} \tag{80}$$

are dimensionless functions. It is worth noting that $k_3^{(1)}$ is a purely geometrical function that accounts for the effect of the opening angle 2α and takes the same form as the homogeneous case, Eq. (20). On the other hand, the other dimensionless function $k_3^{(2)}$ accounts for the effect of the size of the circular regions and their elastic properties on the NSIF. It is interesting to note that this function has the following asymptotic values:

$$\begin{cases}k_3^{(2)}=\dfrac{2\zeta_{BC}}{1+\zeta_{BC}} & \text{for } \zeta_{AC}\to\zeta_{BC} \quad \text{(a)}\\ k_3^{(2)}=\dfrac{4\zeta_{BC}t_2^2}{\left(1+\zeta_{BC}\right)^2t_2^2-\left(1-\zeta_{BC}\right)^2t_1^2} & \text{for } \zeta_{AC}\to1 \quad \text{(b)}\\ k_3^{(2)}=\dfrac{4\zeta_{BC}t_2^2}{\left(1+\zeta_{BC}\right)t_2^2-\left(1-\zeta_{BC}\right)t_1^2} & \text{for } \zeta_{AC}\to\infty \quad \text{(c)}\\ k_3^{(2)}=0 & \text{for } \zeta_{AC}\to0 \quad \text{(d)}\\ k_3^{(2)}=0 & \text{for } \zeta_{BC}\to0 \quad \text{(e)}\\ k_3^{(2)}=\dfrac{2\zeta_{AC}}{1+\zeta_{AC}} & \text{for } \zeta_{BC}\to1 \quad \text{(f)}\\ k_3^{(2)}=0 & \text{for } \zeta_{BC}\to\infty \quad \text{(g)}\\ k_3^{(2)}=\dfrac{2\zeta_{AC}}{1+\zeta_{AC}} & \text{for } t_2\to t_1 \quad \text{(h)}\\ k_3^{(2)}=\dfrac{4\zeta_{AC}\zeta_{BC}}{\left(\zeta_{AC}+\zeta_{BC}\right)\left(\zeta_{BC}+1\right)} & \text{for } t_2\to\infty \quad \text{(i)}\end{cases} \tag{81}$$

Eqs. (81)(d) and (81)(e) show that if any of the circular regions has elastic moduli tending to zero then the dimensionless NSIF will also tend to zero. On the other hand, Eq. (81)(g) indicates that if the outer shell, region Ω^B, is very stiff compared to the outer region then it will shield the tip of the notch from the stresses and the NSIF will also tend to zero. For cases in which the modulus of the first circular region coincides with the modulus of the second region Ω^B or the modulus of the second region coincides with the one of the outer region Ω^C, Eqs. (81)(a) and (81)(f) show that the dimensionless function will tend to $2\zeta_{BC}/(1+\zeta_{BC})$ or $2\zeta_{AC}/(1+\zeta_{AC})$ which combined with $k_3^{(1)}$ give exactly the dimensionless function for the bimaterial case, Eq. (56). As Eq. (81)(h) shows, a similar result is obtained when the radius of the second circular region tends to the radius of the first region, $t_1\to t_2$. Finally, if the first circular region features the same modulus of region Ω^C or if its modulus is significantly larger then the dimensionless function depends on the radii of Ω^A and Ω^B and the ratio $\zeta_{BC}=G_B/G_C$ according to Eqs. (81)(b) and (81)(c).

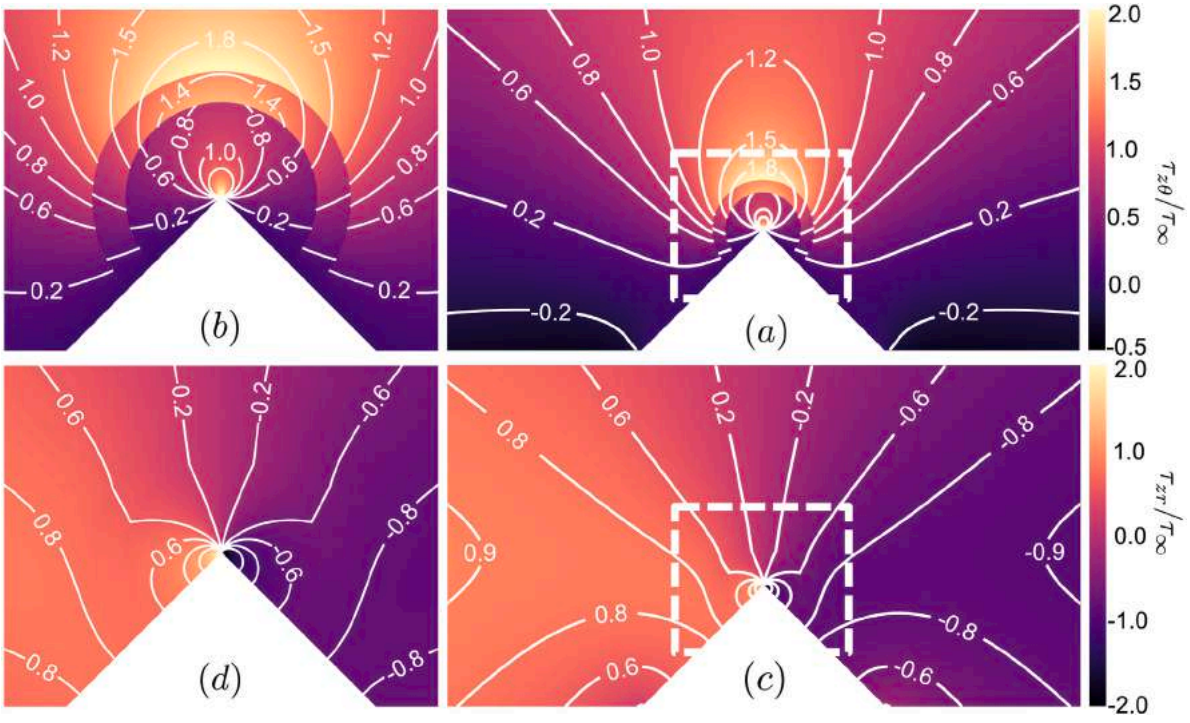

Fig. 18. Normalized stress distribution for a finite V-notch of depth $b = 5$ mm and opening angle $2\alpha = 90°$ with circular regions made of different material of radii $a_1 = 0.3b$ and $a_2 = 0.4b$ embracing the tip. The notch is subjected to a remote stress $\lim_{z\to\infty} \tau_{zx} = -\tau_\infty$. The material inside the circular region Ω^A features a shear modulus $G_A = 1500$ MPa while the material inside the circular region Ω^B features a shear modulus $G_B = 3000$ MPa. The outer region, Ω^C, has a shear modulus $G_C = 4500$ MPa: (a) $\tau_{z\theta}/\tau_\infty$, (b) magnified view, (c) τ_{zr}/τ_∞, and (d) magnified view. Note the discontinuity on $\tau_{z\theta}/\tau_\infty$ on the interface Ω^A–Ω^B and Ω^B–Ω^C while τ_{zr}/τ_∞ is perfectly continuous for equilibrium.

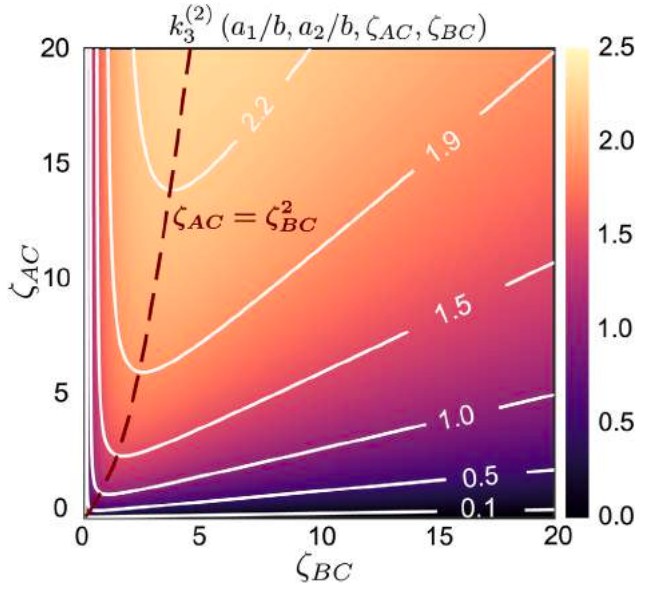

Fig. 19. Contour plot of the dimensionless $k_3^{(2)}\left(a_1/b, a_2/b, \zeta_{AC}, \zeta_{BC}\right)$ as a function of the elastic property ratios $\zeta_{AC} = G_A/G_C$ and $\zeta_{BC} = G_B/G_C$ for $2\alpha = 90°$, $b = 5$ mm, $a_1/b = 0.3$, and $a_2/b = 0.4$.

The foregoing equations enable a thorough investigation of the evolution of the NSIF as a function of the geometrical and material parameters of the problem. Fig. 19 presents a contour plot of $k_3^{(2)}\left(a_1/b, a_2/b, \zeta_{AC}, \zeta_{BC}\right)$ as a function of the elastic parameters of the circular regions, $\zeta_{AC} = G_A/G_C$ and $\zeta_{BC} = G_B/G_C$, for an opening angle $2\alpha = 90°$, a notch depth $b = 5$ mm, $a_1/b = 0.3$, and $a_2/b = 0.4$. As can be noted, the relation between $k_3^{(2)}$ and the material parameters is quite interesting. For a given ratio between the shear modulus of region Ω^B and region Ω^C, decreasing the shear modulus of region Ω^A always leads to a reduction of the dimensionless function and hence the NSIF. This shows that utilizing softer materials in the inner region embracing the notch flanks is an effective way to mitigate the intensity of the stress field close to the tip. On the other hand, for a given ratio ζ_{AC} between the shear modulus of the inner circular region Ω^A and Ω^C, the dependence of the dimensionless function is more complex. For $\zeta_{BC} \le \sqrt{\zeta_{AC}}$, the $k_3^{(2)}$ decreases smoothly with increasing values of ζ_{BC}. In other words, for a constant ζ_{AC}, increasing the stiffness of the outer circular region Ω^B can reduce the NSIF down to a minimum corresponding to the case in which $\zeta_{BC} = \sqrt{\zeta_{AC}}$. For $\zeta_{BC} > \sqrt{\zeta_{AC}}$, increasing the stiffness of the outer circular region can only increase the NSIF. These observations along with Eqs. (78)–(80) provide significant guidance for the effective design of multimaterial notches with low NSIF and potentially higher damage tolerance compared to traditional designs.

A contour plot of $k_3^{(2)}\left(a_1/b, a_2/b, \zeta_{AC}, \zeta_{BC}\right)$ as a function of the sizes of the multimaterial circular regions as expressed by the ratios a_1/b and a_2/b is presented in Fig. 20(a,b) for $2\alpha = 90°$ and $b = 5$ mm.

Fig. 20(a) considers the case in which the inner circular region is softer than Ω^C while the outer circular region is stiffer: $\zeta_{AC} = 1/2$ and $\zeta_{BC} = 2$. It is interesting to note that, for a given size of the outer circular region a_2/b, increasing the radius of the inner region a_1/b leads to an increase in the NSIF. This is explained by the fact that the stiffer outer region tends to partially shield the inner region from the remote stress. By increasing the radius of the inner region, the volume fraction of the outer region decreases leading to a slight increase of the stress intensity close to the tip. For a given a_2/b the maximum increase in the NSIF is obtained when the inner radius tends to the critical value: $a_1/b \to a_2/b$. On the other hand, increasing a_2/b for a given inner radius a_1/b leads to a reduction of the dimensionless function k_3^2, and hence the NSIF. This due to the increase in shielding effect of region Ω^B by increasing its extent.

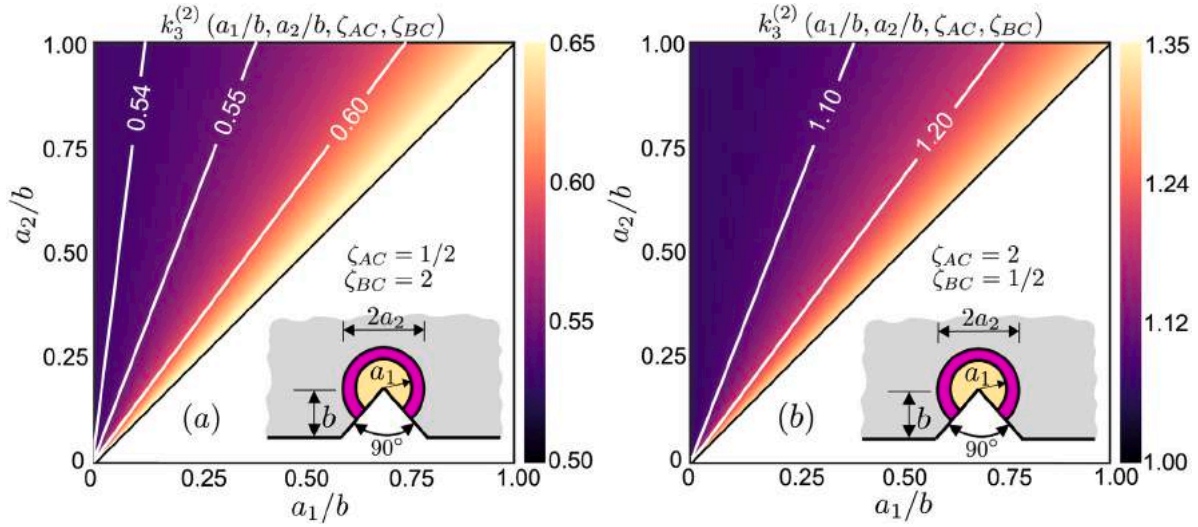

Fig. 20. Contour plots of the dimensionless $k_3^{(2)}(a_1/b, a_2/b, \zeta_{AC}, \zeta_{BC})$ as a function of the radii of the circular regions embracing the tip for two combinations of elastic properties: (a) Ω^A is softer than Ω^C while Ω^B is stiffer than Ω^C, (b) Ω^A is stiffer than Ω^C while Ω^B is softer than Ω^C. For all the cases, $b = 5$ mm and $2\alpha = 90°$.

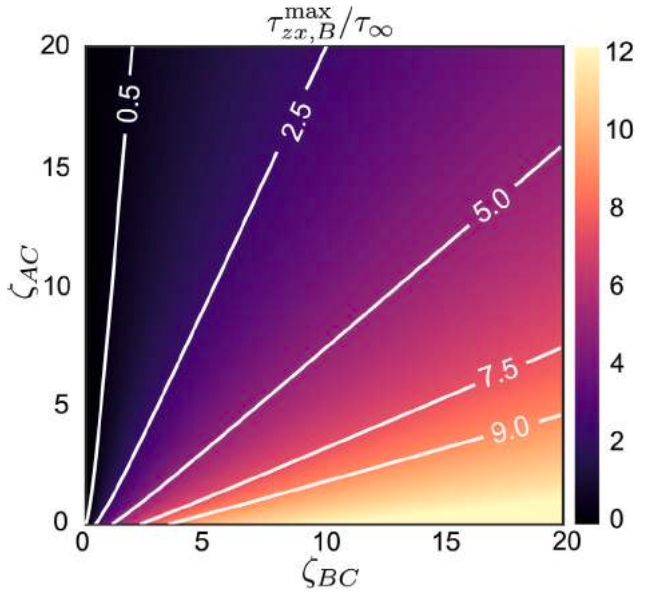

Fig. 21. Contour plot of the stress concentration in region Ω^B as a function of the elastic property ratios $\zeta_{AC} = G_A/G_C$ and $\zeta_{BC} = G_B/G_C$ for $2\alpha = 90°$, $b = 5$ mm, $a_1/b = 0.3$, and $a_2/b = 0.4$.

Fig. 20(b) considers the case in which the inner circular region is stiffer than Ω^C while the outer circular region is softer: $\zeta_{AC} = 2$ and $\zeta_{BC} = 1/2$. The first observation that can be made by comparing (20b) to (20a) is that for any combination of a_1/b and a_2/b, the values of k_3^2 are always large then in the previous case. This confirms that the most effective way to reduce the NSIF is to have softer materials in the region close to the tip. Similar to what was observed before, increasing the size of the outer region while keeping a_1/b constant leads to a reduction of the NSIF. This is again due to an increase in shielding of Ω^A by the outer circular region Ω^B. On the other hand, increasing the size of the inner region while keeping a_2/b constant leads to an increase of the NSIF. These results suggest that it is possible to design the multimaterial domain to mitigate the Notch Stress Intensity Factor (NSIF) without excessively load the other outer regions by finding a suitable combination of a_1/b and a_2/b.

Finally, it is important to note that, thanks to Eqs. (78)–(80), it is possible to calculate the Notch Stress Intensity Factor (NSIF) as a function of the material and geometrical parameters of the problem. Once the NSIF is calculated, the Cartesian stresses near the tip can be calculated taking advantage of Eqs. (21) and (22) while the polar stress components can be calculated using Eqs. (23) and (24).

4.2. Maximum stress in Ω^B

The analysis performed in Section 3 revealed that in addition to the NSIF, also the maximum stress in the other region depends on the material and geometrical parameters of the problem. Soft materials in Ω^A can lead to lower NSIFs but also higher stress concentrations in Ω^B. This can potentially undermine the benefits of reducing the NSIF if the failure is initiated at the point of maximum stress concentration instead of the notch tip. Accordingly, it is important to investigate how the maximum stress in Ω^B is affected by the material and geometrical configurations now that there are three regions made of different materials instead of only two. Towards this goal, it is useful to note that $v_1 = u_1 = u_v = 0$ at the point of maximum stress. Considering Eq. (25), this means that $v_v = t_1$ in the location of maximum stress. Inserting this result into Eq. (73) and extracting the real part of the equation leads to the following expression for the maximum stress:

$$\tau_{zx,B}^{max} = \frac{4\tau_\infty \zeta_{BC}^2 t_2^2}{(\zeta_{AC} - \zeta_{BC})(\zeta_{BC} - 1) t_1^2 + (\zeta_{AC} + \zeta_{BC})(\zeta_{BC} + 1) t_2^2} \times \left(\frac{\sqrt{t_1^2 + 1}}{t_1} \right)^{1 - \frac{2\alpha}{\pi}} \tag{82}$$

It is interesting to note that the foregoing equation differs from the homogeneous case, Eq. (31), only for a multiplying factor. As expected, when $\zeta_{AC} \to 0$ and $\zeta_{BC} \to 1$ the stress concentration tends to the homogeneous case of V-notch with a circular end hole of radius a_1.

Fig. 21 provides a contour plot of the stress concentration factor, $\tau_{zx,B}^{max}/\tau_\infty$, as a function of the elastic property ratios $\zeta_{AC} = G_A/C_C$ and $\zeta_{BC} = G_B/C_C$ for a given opening angle $2\alpha = 90°$, $b = 5$ mm, $a_1/b = 0.3$, and $a_1/b = 0.4$. As can be noted, there is a strong dependence of the stress concentration on the elastic parameters. In particular, for a given ζ_{BC}, increasing the ratio between the shear modulus of the inner circular region Ω^A and the shear modulus of Ω^C always leads to a reduction of the stress concentration. This result can be explained by considering that increasing the stiffness of Ω^A allows this region to

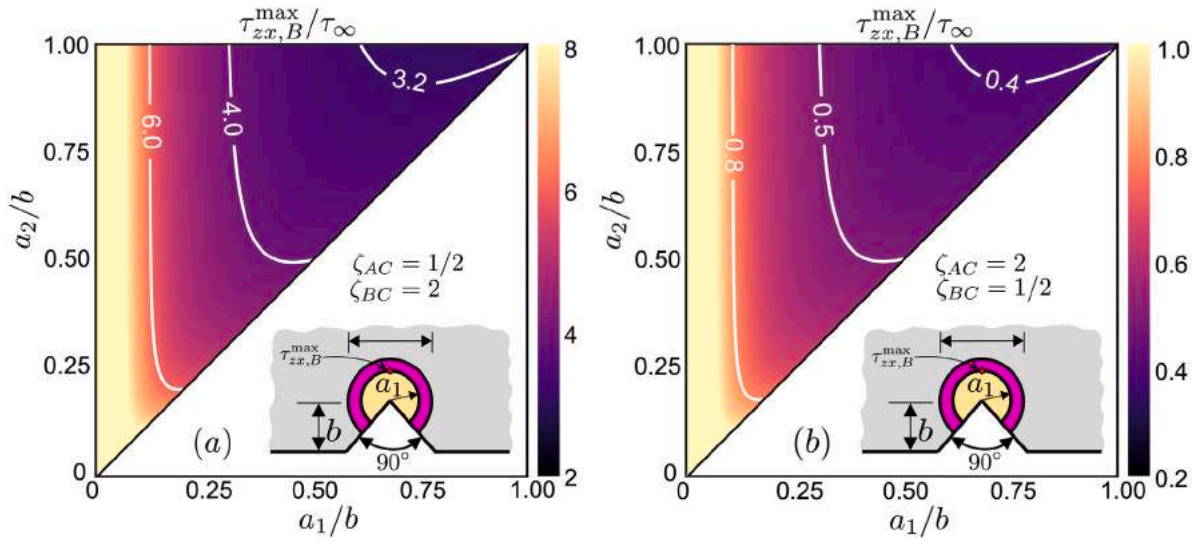

Fig. 22. Contour plots of the stress concentration in region Ω^B as a function of the radii of the circular regions embracing the tip for two combinations of elastic properties: (a) Ω^A is softer than Ω^C while Ω^B is stiffer than Ω^C, (b) Ω^A is stiffer than Ω^C while Ω^B is softer than Ω^C. For all the cases, $b = 5$ mm and $2\alpha = 90°$.

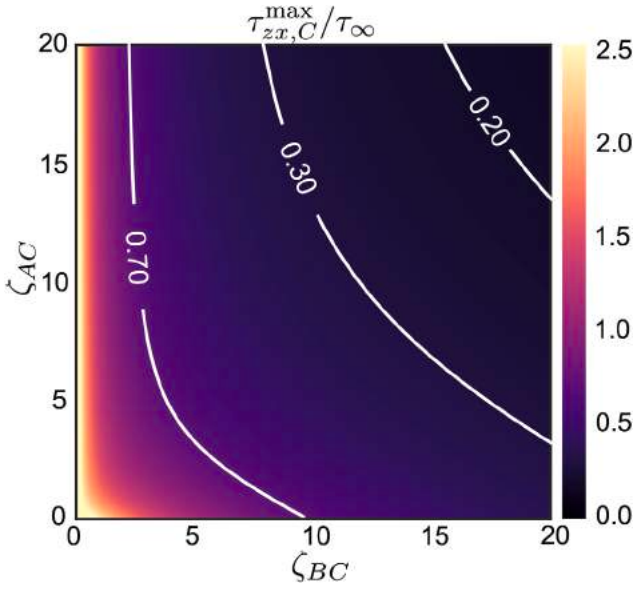

Fig. 23. Contour plot of the stress concentration in region Ω^C as a function of the elastic property ratios $\zeta_{AC} = G_A/G_C$ and $\zeta_{BC} = G_B/G_C$ for $2\alpha = 90°$, $b = 5$ mm, $a_1/b = 0.3$, and $a_2/b = 0.4$.

take more load hence relieving the stresses in Ω^B. On the other hand, increasing the stiffness of Ω^B while keeping ζ_{AC} constant always leads to an increase of the stress concentration. This result is particularly important because it was shown in the previous section that one of the most effective ways to reduce the NSIF is to increase the shear modulus of Ω^B. However, Fig. 21 clearly shows that this leads to an increase of the stress concentration in the region. A conclusion that can be drawn here is that, in order to increase the overall capacity of the structure, the combination of material properties of the regions embracing the notch will need to be selected carefully to make sure that by reducing the NSIF one does not trigger an unwanted failure in Ω^B.

Fig. 22(a,b) show the effects on the stress concentration in Ω^B of the radii of the circular regions Ω^A and Ω^B for an opening angle $2\alpha = 90°$, $b = 5$ mm, and two combinations of elastic properties. Fig. 22(a) considers the case in which the inner circular region Ω^A is softer than Ω^C while the outer circular region Ω^B is stiffer: $\zeta_{AC} = 1/2$ and $\zeta_{BC} = 2$. It can be noted that for a given a_1/b increasing the radius of the outer circular region always leads to a decrease of the stress concentration in Ω^B. On the other hand, for a given a_2/b increasing the inner radius generally leads to a decrease of the stress concentration except for cases in which both a_1/b and a_2/b are very close to 1 (upper right portion of the contour plot). Intuitively, this can be explained by considering the extreme case in which $\zeta_{AC} \to 0$. This would correspond the case of a V-notch with an end hole of radius a_1 and a circular shell of shear modulus G_B and radius a_2 surrounding it. Increasing the radius a_1 would reduce the sharpness of the notch decreasing the stress concentration. Although the case represented in Fig. 22(a) is not as extreme and $\zeta_{AC} = 1/2$, the same trend can be noted. Similar conclusions can be drawn from Fig. 22(b) which describes the case in which the inner region Ω^A is stiffer than Ω^C while the outer circular region Ω^B is softer: $\zeta_{AC} = 2$ and $\zeta_{BC} = 1/2$. The main difference compared to the previous case is that, for given a_1/b and a_2/b, the use of a soft material in region Ω^B in lieu of a stiff material reduces significantly the stress concentration.

4.3. Maximum stress in Ω^C

The calculation of the maximum stress in Ω^C can be done following the same procedure outlined in Section 4.2. This time, it is useful to note that in the position of maximum stress $u_2 = v_2 = 0$ while $u_1 = 0$. Leveraging Eq. (58) it is easy to show that this means that:

$$v_1 = \frac{t_2^2 - t_1^2}{t_2} \tag{83}$$

at the location of maximum stress. Substituting this result into Eq. (74), introducing Eqs. (67) and (68), and taking the real part leads to the following equation for the maximum stress:

$$\begin{aligned}\tau^{max}_{zx} &= \left(M\frac{t_1^2+t_2^2}{t_2^2} + 2G\right)\left(\frac{\sqrt{t_2^2+1}}{t_2}\right)^{1-\frac{2\alpha}{\pi}} \\ &= \frac{2\tau_\infty\left[\left(\zeta_{BC}-\zeta_{AC}\right)t_1^2 + \left(\zeta_{BC}+\zeta_{AC}\right)t_2^2\right]}{\left(\zeta_{AC}-\zeta_{BC}\right)\left(\zeta_{BC}-1\right)t_1^2 + \left(\zeta_{BC}+\zeta_{AC}\right)\left(\zeta_{BC}+1\right)t_2^2} \\ &\quad\times\left(\frac{\sqrt{t_2^2+1}}{t_2}\right)^{1-\frac{2\alpha}{\pi}}\end{aligned} \tag{84}$$

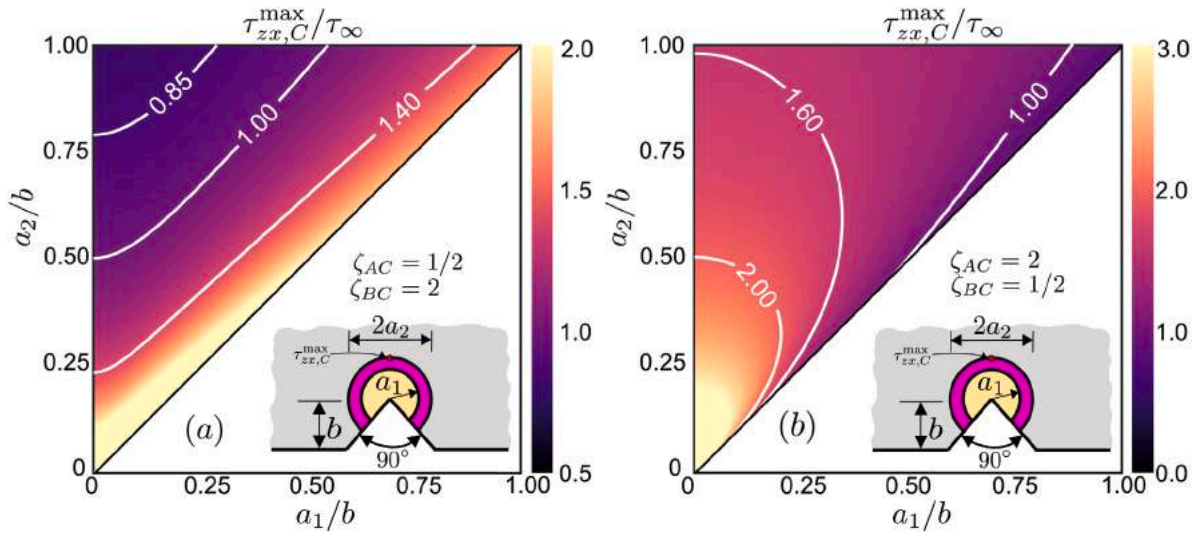

Fig. 24. Contour plots of the stress concentration in region Ω^C as a function of the radii of the circular regions embracing the tip for two combinations of elastic properties: (a) Ω^A is softer than Ω^C while Ω^B is stiffer than Ω^C, (b) Ω^A is stiffer than Ω^C while Ω^B is softer than Ω^C. For all the cases, $b = 5$ mm and $2\alpha = 90°$.

The foregoing equation is very similar to the homogeneous case except for a multiplying factor that depends on the interplay between the radii of the circular regions and their elastic shear moduli. It is worth noting that for $\zeta_{AC} \to \zeta_{BC} \to 0$ the stress concentration tends to the one of a V-notch with an end hole of radius a_2. On the other hand, the case $\zeta_{AC} \to \zeta_{BC}$ leads to the same stress concentration of the bimaterial case discussed in Section 3.

To investigate more thoroughly the effects of the mechanical and geometrical parameters of the problem on the stress concentration in Ω^C, Fig. 23 shows $\tau_{zx,C}^{max}/\tau_\infty$ as a function of the elastic parameters ζ_{AC} and ζ_{BC} for an opening angle $2\alpha = 90°$, a depth $b = 5$ mm, $a_1/b = 0.3$, and $a_2/b = 0.4$. As can be noted, the elastic parameters have a very significant effect on the stress concentration. In particular, it is worth noting that for a given ζ_{BC}, increasing the elastic modulus of the inner circular region Ω^A tends to reduce the stress concentration in region Ω^C. This is because, for a given remote stress τ_∞, increasing the modulus of Ω^A increases the load taken by such region thus relieving part of the stress concentration in Ω^C. Similarly, for a given ζ_{BC}, increasing the modulus of the outer circular region Ω^B always reduces the stress concentration in Ω^C. This is again due to the increased load taken by Ω^B which leads to a decrease of the stresses in the other two regions.

Fig. 24(a,b) show the stress concentration $\tau_{zx,C}^{max}/\tau_\infty$ as a function of a_1/b and a_2/b for an opening angle $2\alpha = 90°$, a notch depth $b = 5$ mm, and two combinations of elastic parameters. In particular, Fig. 24(a) shows the case in which the inner circular region is softer than Ω^C while the outer circular region Ω^B is stiffer: $\zeta_{AC} = 1/2$ and $\zeta_{BC} = 2$. From the figure, it can be noted that, for a given a_1/b, increasing the size of the outer circular region Ω^B always leads to a reduction of the stress concentration in Ω^C. This is because the volume fraction of material with a high shear modulus increases. This more load can be taken by ω^B relaxing part of the stresses in Ω^C. On the other hand, for a given a_2/b, increasing the radius of the inner circular region always increases the stress concentration. This is because, increasing the radius of Ω^A, the volume fraction of softer material increases. This means that more load has to be taken by the other two region with the result that the stress concentration in Ω^C increases.

Fig. 24(b) shows the case in which the inner circular region is stiffer than Ω^C while the outer circular region Ω^B is softer: $\zeta_{AC} = 2$ and $\zeta_{BC} = 1/2$. Similar to the previous case, it can be noted that increasing the size of the outer circular region Ω^B for a given a_1/b tends to reduce the stress concentration. On the other hand, for a given a_2/b, larger radii of the inner circular region Ω^A lead to a decrease of the stress concentration. This trends, opposite to the one presented in (24a), is explained by the fact that the inner region is stiff in this case. Hence, increasing its radius increases the volume fraction of stiff material that can take more load and relieve region Ω^C from some of the stress.

5. Nonlinear computational modeling

The analytical study presented in Sections 3 and 4 was performed within the framework of Linear Elastic Fracture Mechanics (LEFM). One of the fundamental hypotheses of LEFM is that the material is brittle so that the sizes of the Plastic and Fracture Process Zones are negligible compared to the portion of the structure that still behaves elastically. Such conditions are met also by materials such as high-strength steel which might exhibit some plasticity at the notch tip but obey to the conditions of small-scale yielding. The fact that most of the structure still behaves elastically makes the Notch Stress Intensity Factor (NSIF) still an accurate parameter to describe the process of failure. However, when the small-scale yielding condition is not met or when the materials exhibit complex quasibrittle behavior, the NSIF might not be enough to describe the failure process. This is because the size of the Plastic Zone or the Fracture Process Zone is not negligible for these materials and the stresses inside these regions can be highly nonlinear (Bažant et al., 2021). The NSIF cannot account for any nonlinearity since it was derived based on the assumption of linear elastic behavior.

Extensive studies from the literature have pointed out that materials that behave in a relatively brittle way under plane loading conditions can exhibit more ductile behavior under antiplane shear. Berto et al. (2012), for instance, reported significant plastic deformations in torsion tests at room temperature on notched specimens made of polymethyl methacrylate (PMMA), which is generally considered a rather brittle material. In light of this, it is important to investigate the structural behavior using nonlinear computational modeling to understand if the reduction of the NSIF using the multimaterial concept presented in this work can still lead to an increase in structural capacity even in the presence of the enhanced ductility induced by the Mode III loading. In fact, in such scenario, it is not guaranteed that the concept would work or would be as effective. For instance, if the induced ductility is enough to generate a large plastic zone in front of the notch already in the single-phase system, there is a possibility that this would already significantly reduce the severity of the notch. At this point, having a multimaterial configuration might not be effective compared to the single-phase case since the "blunting" of the sharp V-notch is already

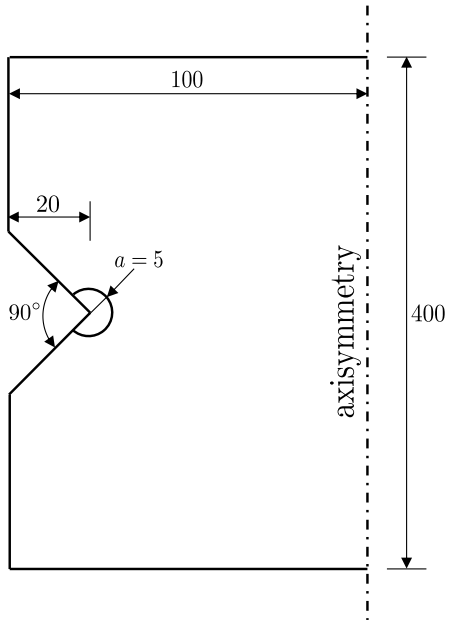

Fig. 25. Circular shaft weakened by a finite V-notch under torsion investigated in this work. All the dimensions are in mm.

performed by the plastic stresses rather than the circular region. Hence, the motivation for the computational study is to investigate if the NSIF reduction is still enough to lead to a significant increase in the capacity of the structure.

Towards this goal, this section focuses on the nonlinear computational modeling of the proposed multimaterial system. As a case study, a circular shaft featuring a finite V-notch under torsion was investigated. For simplicity, only two configurations were analyzed. The first configuration is the homogeneous case, where the system is made of an epoxy polymer, a material commonly used in additive manufacturing. This is used as a benchmark to evaluate the performance of the second configuration which is a bimaterial system like the one shown in Fig. 3 where a circular region of radius a is made of vulcanized rubber while the rest of the structure is made of epoxy. As can be noted from Fig. 25, which provides all the geometrical details of the problem, the circular shaft has a radius 100 mm and a length of 400 mm and it features a V-notch of opening angle $2\alpha = 90°$ and depth $b = 20$ mm. A circular partition of radius $a = 5$ mm centered at the tip of the notch and embracing it was created to allow the assignment of a different material behavior.

It is worth mentioning that this section serves the only purpose of validating the performance of the proposed multimaterial system in the presence of realistic inelastic deformation. No optimization studies were performed to identify the ideal combination of radii and material properties. Furthermore, only a system composed of a soft and an hard phase was investigated. It is likely that thorough optimization studies can lead to more significant differences between the performance of homogeneous and the bimaterial system. However, this is beyond the scope of the present study.

5.1. Finite element model

For the nonlinear simulation of the torsion problem a finite element model was created in ABAQUS/Explicit. In order to allow the fracture pattern to be non-axisymmetric, a full three-dimensional problem was solved in ABAQUS/Explicit as shown in Fig. 26(a,b). A mesh of 926,223 hexahedral elements with reduced integration was used to accurately resolve the stress and strain fields. As the insert in Fig. 26(a) shows, particular care was devoted to getting a very regular and fine mesh close to the notch tip. A thorough convergence study confirmed that this allowed an objective description of the stress and strain fields before localization. On the other hand, as described in Appendices B and C, mesh objective results in the presence of localization were guaranteed by the use of the crack band model at the constitutive level (Bažant and Oh, 1983; Bažant and Planas, 1997; Bažant et al., 2021). To simulate the behavior of epoxy and vulcanized rubber elasto-plastic-damage and hyperelastic-damage models were implemented as user subroutine in ABAQUS/Explicit. The details of the models are provided in Appendices B and C. To capture possible delamination at the rubber/epoxy interface, the ABAQUS cohesive interaction algorithm with a linear mixed-mode traction separation law was used. The interface was assumed to have a normal strength of 50 MPa and a shear strength of 15 MPa. The Benzeggagh and Kenane (1996) mixed-mode initiation criterion was used with an exponent of 2.

For the application of the boundary conditions, two reference points were assigned at the center of the top and bottom surfaces respectively. A tie constraint to the reference point at the top was assigned to all the nodes on the top surface while the nodes of the bottom surface were tied to the reference point at the bottom. To simulate a torsional load, the reference point at the bottom was completely fixed. The simulation was performed in rotation-control by applying a linearly increasing rotation along the axis, θ, on the top reference point and measuring the reaction torque, T. A typical von Mises stress distribution at peak load for the bimaterial case is shown in Fig. 26(b) as an example.

5.2. Discussion on possible failure scenarios

The simplest failure scenario is when both the material in the circular region and the material outside of it are extremely brittle. In such a case, the nonlinear Plastic Zone and Fracture Process Zone are small compared to the geometrical dimensions of the problem. The brittle failure can independently be triggered either in the material at the tip of the V-notch (material A) or in the material at the maximum stress location at the tip of the circular region (material B). Initiation at the V-notch will occur if the NSIF reaches a critical value, K_{3c}, for material A before the maximum stress outside the circular region reaches the strength of material B, σ_t. Vice versa, in case the maximum stress in Material B reaches the strength before the NSIF in material A reaches K_{3c}, the initiation will occur directly at the tip of the circular region. In summary, for purely brittle materials it is almost straightforward to describe the failure process and increase the structural capacity. The key is to select a material in the circular region so that the multimaterial combination reduces the NSIF without increasing excessively the stress concentration in material B. Furthermore, if the material A can also be selected so that it features a larger K_{3c}, this would contribute to a larger capacity.

Now, if materials A and B are elasto-plastic instead of very brittle the fracture becomes significantly more complicated. If the base material features already large ductility, the large Plastic Zone forming at the tip of the V-notch may contribute already to the reduction of the intensity of the stress field. Furthermore, the PZ can also contribute to additional energy dissipation upon failure. At this point, adding a circular region of a different material might not lead to significant benefits in terms of structural capacity. In fact, if the PZ is large enough to cover the circular region, the reduction on the stress intensity at the V-notch due to the elastic deformation might be even lower than the one induced by the plastic deformations.

In case both materials A and B are quasibrittle and the FPZ is small enough compared to the size of the circular region and the depth of the V-notch, the failure process gets even more complex. In fact, prior to reaching the critical load of the structure, the FPZ will be partially developed in both material A and B. If the failure starts in the material B and the FPZ in material A is fully developed then the fracture energy dissipated by material A will also contribute to the fracture process. Hence, utilizing a tougher material in the circular region might help

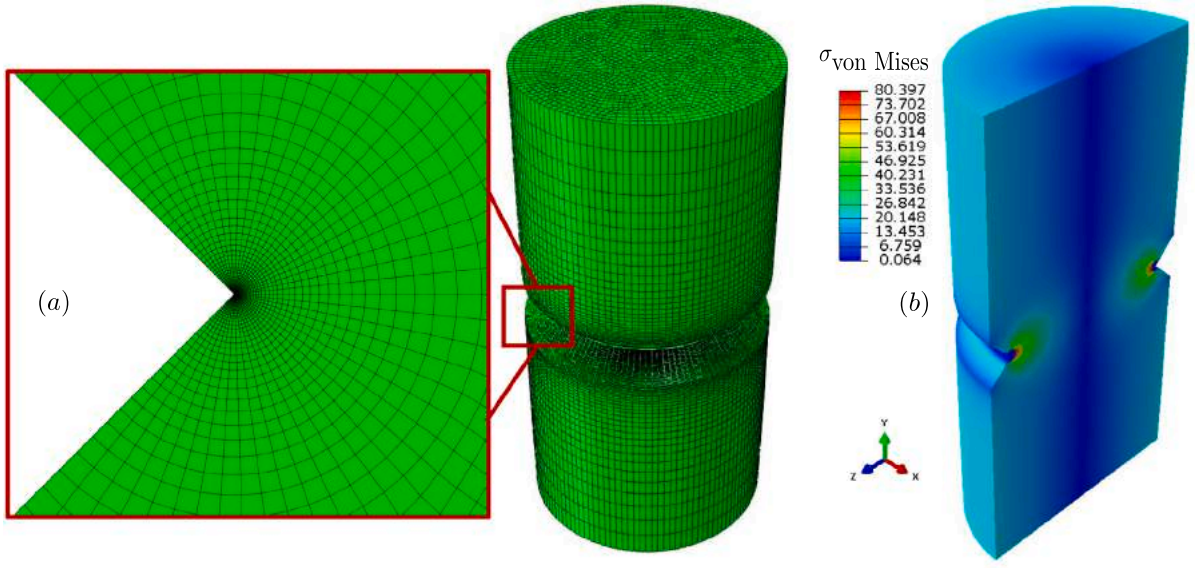

Fig. 26. FE model of the circular shaft weakened by a finite V-notch under torsion: (a) FE mesh with 926,223 hexahedral elements (the insert shows a magnification of the mesh at the notch tip), (b) von Mises stress distribution for the bimaterial system at peak load.

increasing the structural capacity. On the other hand, if when the failure starts in material B the FZP in material A is not developed, then fracture energy of material A will have a minimum contribution to the capacity of the structure. In other words, in such case, using a very tough material in region A will not contribute much to an increase in structural capacity.

5.3. Results and discussion

Thanks to the nonlinear computational models it was possible to investigate the structural behavior of the homogeneous and bimaterial systems under torsion. As mentioned in the foregoing sections, the bimaterial system featured a circular region surrounding the notch tip made of vulcanized rubber while the rest of the structure was made of epoxy. Rubber was chosen since the linear elastic solution for the NSIF showed that the use of soft materials at the tip can help reduce the stress intensity. In addition, rubber features a very large fracture energy compared to epoxy which helps achieving higher ultimate loads.

The results of the simulations are summarized in Fig. 27 which shows the torque as a function of the torsion angle for the two configurations investigated. As can be noted, the addition of a soft phase to mitigate the intensity of the stress field indeed improves the performance of the structure. In fact, it is worth noting that the structural capacity of the bimaterial system made of rubber and epoxy is almost 50% higher of the homogeneous system made of epoxy. At the same time, the blunting of the notch enabled by the soft phase seems to promote large plastic deformations before reaching the peak load. This translates into a larger rotation at failure which is almost 90% higher than the homogeneous case. Another interesting result shown in Fig. 27 is that, since the soft phase occupies only a very limited region surrounding the notch tip, the overall stiffness of the structure decreases of only 8% compared to the homogeneous case. This is an additional benefit considering that several other approaches to increase the capacity and damage tolerance of structural components often lead to a significant stiffness loss. It is worth stressing here again that the circular region was made of a hyperelastic medium which unloads to zero. In other words, the additional phase did not feature any permanent deformation in contrast to ductile materials. This means that no energy dissipation occurred in the circular region prior to fracture. The only plastic dissipation could occur in the epoxy phase. In this context, the fact that the capacity is increased is all but guaranteed. The

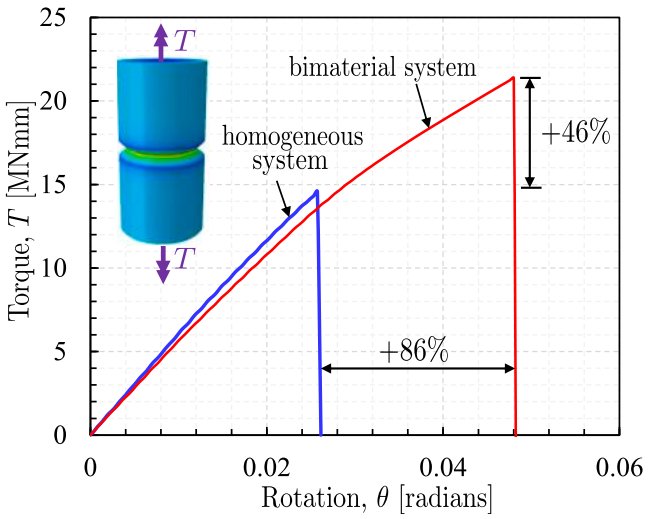

Fig. 27. Nonlinear simulation of the structural response (Torque vs rotation angle) for the case of a homogeneous structure and a bimaterial notch. Note that the addition of a soft phase in front of the notch increases the structural capacity of 46% while the rotation at failure is increased of 86% compared to the homogeneous case.

simulation presented in this work showed that, at peak, no cohesive zone was able to form in the rubber. The failure occurred when the Fracture Process Zone (FPZ) in the epoxy phase reached a critical value after which unstable crack propagation occurred. In such scenario, the fact that rubber features a larger fracture energy compared to epoxy did not contribute to the increase in structural capacity. The main reason for the increase in capacity is that with the addition of a very complaint circular region the failure was forced to happen in epoxy by the formation of a large FPZ ahead of the blunt notch rather than a sharp V-notch.

Finally, it is worth stating here again that the goal of the nonlinear simulations was to demonstrate the validity of the proposed multimaterial system in increasing the structural capacity also in the presence of realistic inelastic strains. It is expected that different material combinations as well as geometrical configurations can lead to different results. It is also envisioned that the use of multiple circular regions

like shown in Fig. 17 instead of just one can lead to higher tunability of the system and enhanced performance. Thorough optimization studies can lead to even larger gains in performance compared to the simple case investigated in this work. However, this was not in the scope of the present work and it will be the subject of future studies.

6. Conclusions

This study investigated the addition of circular regions embracing the tip of finite V-notches to reduce the Notch Stress Intensity Factor (NSIF) and increase the capacity of structures subjected to antiplane shear and torsion. Towards this goal, a general framework for finding the closed-form solution for stresses, displacements, and NSIFs was presented for the first time. Moreover, nonlinear simulations using elasto-plastic-damage and hyperelastic-damage models were performed to investigate the increase of structural capacity.

Based on the results presented in this work it is possible to elaborate the following conclusions:

1. The stress and displacement distributions for finite V-notches featuring N circular regions of different materials embracing the tip under antiplane shear and torsion can be calculated in closed-form by combining the solutions of N homogeneous sub-problems. The first sub-problem is a homogeneous finite V-notch with the same depth and opening of the original problem. Each of the other $N-1$ sub-problems is a finite V-notch with a circular end hole of radius corresponding to the circular region surrounding the notch in the original problem. Once the N solutions are combined, the remaining parameters can be uniquely identified by imposing the compatibility conditions on the interfaces and the remote stress condition.
2. For the proposed configuration, the multimaterial regions do not affect the order of the singularity of the stress field close to the tip which, like in the homogeneous case, depends only on the opening angle of the notch: $\sigma_{ij} \propto 1/r^{1-\lambda_3}$ with r = distance from the notch tip, $\lambda_3 = \pi/(2\pi - 2\alpha)$, and 2α = notch opening angle. This is in stark contrast to the case in which the bimaterial interface does not embrace the notch (see e.g. Bogy 1971, Hein and Erdogan 1971, Yu et al. 2010, Le et al. 2010).
3. The Notch Stress Intensity Factor (NSIF) and the stress concentrations at the material interfaces are shown to be significantly influenced by the combination of material properties and radii of the circular regions. For the bimaterial case, the NSIF decreases with decreasing ratios between the shear modulus of the region surrounding the notch tip and the one of the outer region. In contrast, the stress concentration at the bimaterial interface increases. This shows that it is possible to decrease the intensity of the stress field by using softer materials close to the notch tip. However, particular care must be devoted to avoid excessive stress concentrations which can trigger early failures at the material interfaces. For the multimaterial case, the NSIF and stress concentration factors show a complex dependence on a combination of elastic moduli and region radii.
4. A significant advantage of the closed-form solution presented in this work compared to numerical approaches is that it allows to explicitly account for the effects of all the material and geometrical parameters of the problem on the NSIFs and the stress concentrations. This makes it a valuable tool for design of multimaterial structures under antiplane shear and torsion.
5. Advanced hyperelastic-damage and elasto-plastic-damage computational models confirmed the benefits of the proposed multimaterial system also in the presence of nonlinear deformations. Investigating a bimaterial system under torsion made of vulcanized rubber and epoxy showed that the structural capacity can be effortlessly increased of almost 50% while the nominal rotation at failure can be increased of almost 90% compared to the homogeneous case. Since the soft region is limited to the notch tip, the foregoing results are obtained at the expenses of a structural stiffness reduction of only 8%. It is expected that even larger benefits can be achieved by performing thorough optimization studies.
6. It is expected that a similar approach to increase the structural capacity and damage tolerance can be extended to other loading conditions including Mode I and II. Furthermore, it is expected that the proposed system can be used to significantly increase the fatigue life of notched structural components. Considering the low stresses in high-cycle fatigue and the fact that most of the life is spent in damage initiation, it is probably possible to avoid the use of nonlinear computational models and rely completely on the closed-form solution presented in this work for design. The proposed solution e.g. can be used within the Strain Energy Density (SED) fatigue failure criterion by Lazzarin and co-workers which has been extremely successful in the description of high-cycle fatigue failure for a number of brittle material systems (Lazzarin and Zambardi, 2001; Lazzarin et al., 2008; Berto and Lazzarin, 2009).

Declaration of competing interest

The authors declare that they have no known competing financial interests or personal relationships that could have appeared to influence the work reported in this paper.

Acknowledgments

The author acknowledges the financial support from the National Science Foundation, USA under Grant No. CMMI-2032539.

Appendix A. Stress concentration for a finite V-notch with end hole

In Section 2.5.1, a very simple closed-form equation for the calculation of the stress concentration in finite V-notches with end holes was provided for the first time. As can be noted in Eq. (31), such expression indicates that the stress concentration depends on the notch opening angle 2α and the ratio between the notch root radius a and the notch depth b via the parameter t.

For practical design consideration, it is desirable to express the stress concentration as an explicit function of a/b. For $a/b \in [0, 0.1]$, such relationship can be obtained by imposing the condition for the notch tip, $\xi = 0$, and expanding Eq. (26) in Taylor series around $t = 0$:

$$Z(0,t) = i\frac{\pi A_v}{2(\pi-\alpha)} t^{\frac{2(1-\alpha)}{\pi}} + \mathcal{O}\left(t^{4-\frac{2\alpha}{\pi}}\right) \tag{A.1}$$

Then, after retaining only the first term of the equation, imposing the condition that $Z = i(a+b)$, and rearranging, one can find a direct relationship between the parameter t and the shape ratio a/b:

$$t \approx \left[\frac{2(\pi-\alpha)}{\pi A_v/b}\rho\right]^{\frac{\pi}{2\pi-2\alpha}} \qquad \text{for } \rho = \frac{a}{b} \in [0, 0.1] \tag{A.2}$$

For $a/b \in (0.1, 1]$, the following polynomial approximation can be used:

$$t \approx c_3\rho^3 + c_2\rho^2 + c_1\rho + c_0 \qquad \text{for } \rho = \frac{a}{b} \in (0.1, 1] \tag{A.3}$$

This expression was obtained by best fitting of numerical results obtained from Eq. (26). Table A.1 provides a summary of the coefficients c_i used in Eq. (A.3) for various notch opening angles while Fig. A.28(a,b) show the relation between the parameter t and $\rho = a/b$. The symbols represent the exact solution solved numerically by means of Eq. (26) while the solid lines show the excellent approximation provided by Eqs. (A.2) and (A.3).

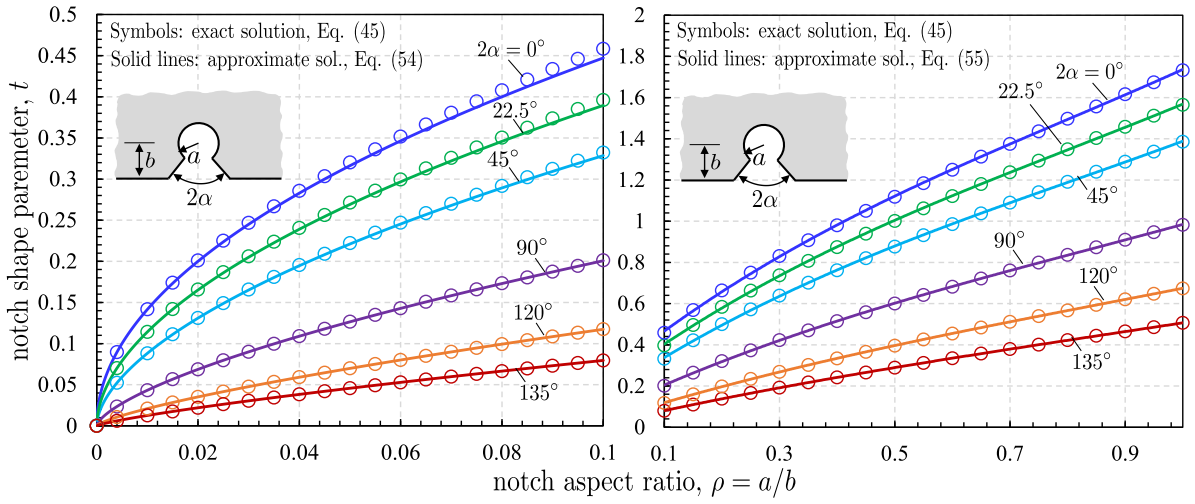

Fig. A.28. Notch shape parameter t used in Eq. (26) as a function of the ratio between notch depth and radius, $\rho = a/b$.

Table A.1
Coefficients c_i of Eq. (A.3) as a function of the notch opening angle.

Opening angle, 2α	c_3	c_2	c_1	c_0
0°	5.71×10^{-1}	-1.37×10^{0}	2.28×10^{0}	2.52×10^{-1}
22.5°	5.14×10^{-1}	-1.24×10^{0}	2.09×10^{0}	2.07×10^{-1}
45°	4.47×10^{-1}	-1.09×10^{0}	1.87×10^{0}	1.62×10^{-1}
90°	2.78×10^{-1}	-6.99×10^{-1}	1.33×10^{0}	7.88×10^{-2}
120°	1.49×10^{-1}	-3.90×10^{-1}	8.80×10^{-1}	3.50×10^{-2}
135°	8.91×10^{-2}	-2.40×10^{-1}	6.38×10^{-1}	1.90×10^{-2}

Appendix B. Elasto-plastic-damage model

The structure investigated in this work is assumed to be made of epoxy, a thermoset polymer that can exhibit significant plastic behavior followed by strain softening. Several seminal studies which investigated the behavior of epoxy polymers under significant biaxial and triaxial stress conditions have shown that yielding strongly depends on the interplay between hydrostatic and deviatoric components of the stress field (see e.g. Asp et al., 1995, 1996). This is confirmed by the fact that the yielding stress in uniaxial tension is generally lower than the yielding stress in uniaxial compression (Werner and Daniel, 2014; Poulain et al., 2014; Hu et al., 2003; Xia et al., 2003). Recently, it was also shown that the hydrostatic stress strongly affects the strain at failure (Qiao et al., 2020). Furthermore, the hydrostatic stress has been shown to affect the ultimate stress. This has led to the development of a number of different failure criteria that account for the effect of the volumetric stress including e.g. Christensen's failure criterion for glassy polymers (Christensen, 2013), the paraboloidal yielding/failure criterion (Tschoegl, 1971; Raghava et al., 1973) or the adaptation of other models such as Drucker–Prager model (Canal et al., 2009) and Mohr–Coulomb (González and LLorca, 2007) to simulate polymers. For large dilatational stresses, it was shown that the failure of the polymer occurs by microcavitation and the Dilatational Energy Density (DED) criterion provides a superior prediction of the failure behavior (Asp et al., 1996). For an interesting recent comparison between some of the foregoing failure criteria to predict the failure initiation in the matrix of fiber composites, the reader is referred to (Kumagai et al., 2020).

For the loading conditions investigated in this work the dilatational stress is not significant and failure by microcavitation is very unlikely. Accordingly, the yield surface of the polymer is assumed to follow the paraboloidal criterion (Tschoegl, 1971; Raghava et al., 1973):

$$f_\sigma\left(\boldsymbol{\sigma}, \sigma_{yc}, \sigma_{yt}\right) = 6J_2 + 2\left(\sigma_{yc} - \sigma_{yt}\right) I_1 - 2\sigma_{yc}\sigma_{yt} \tag{B.1}$$

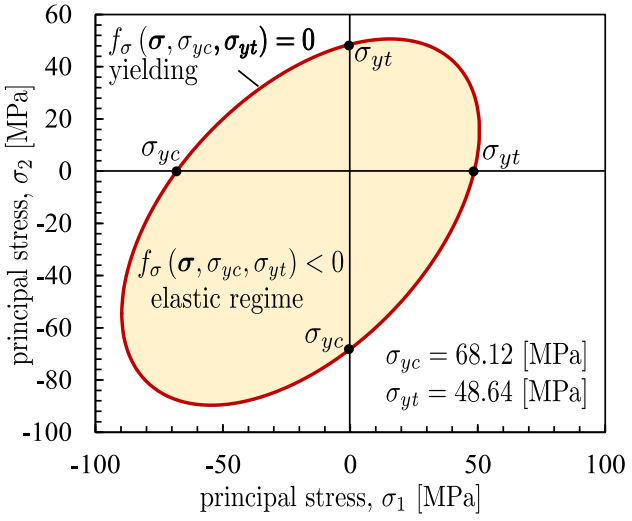

Fig. B.1. Example of biaxial yield surface, $(\sigma_3 = 0)$, predicted by the paraboloidal criterion (Tschoegl, 1971; Raghava et al., 1973).
Source: Yielding stresses taken from (Poulain et al., 2014).

where σ_{yt} and σ_{yc} are the absolute values of the tensile and compressive yield stresses, $J_2 = \frac{1}{2} s_{ij} s_{ij}$ is the second invariant of the deviatoric stress tensor $\boldsymbol{s}$ (note that repeated indexes imply summation), and $I_1 = \mathrm{Tr}(\boldsymbol{\sigma})$ is the first stress invariant. Fig. B.1 exemplifies the biaxial yield surface for $\sigma_{yt} = 48.64$ MPa and $\sigma_{yc} = 68.12$ MPa which are typical values of the initial yield stresses in tension and compression for epoxy (Poulain et al., 2014). This model has been shown to capture the multiaxial behavior of thermosets extremely well except for cases of large dilatational stresses (Asp et al., 1996).

To avoid positive volumetric strain under hydrostatic pressure, a non-associative flow rule characterized by the following plastic potential is used in this work:

$$g_\sigma(\boldsymbol{\sigma}) = \sigma_{vM}^2 + \alpha p^2 \tag{B.2}$$

with $\sigma_{vM} = \sqrt{3J_2}$ = von Mises equivalent stress, $p = 1/3 I_1$ = hydrostatic pressure, and $\alpha = 9/2\left(1 - 2\nu_p\right) / \left(1 + \nu_p\right)$ with ν_p = plastic Poisson's ratio. Then, the non-associative flow rule reads (Jirasek and Bazant, 2001):

$$\Delta\boldsymbol{\varepsilon}^p = \Delta\lambda \frac{\partial g_\sigma}{\partial \boldsymbol{\sigma}} \tag{B.3}$$

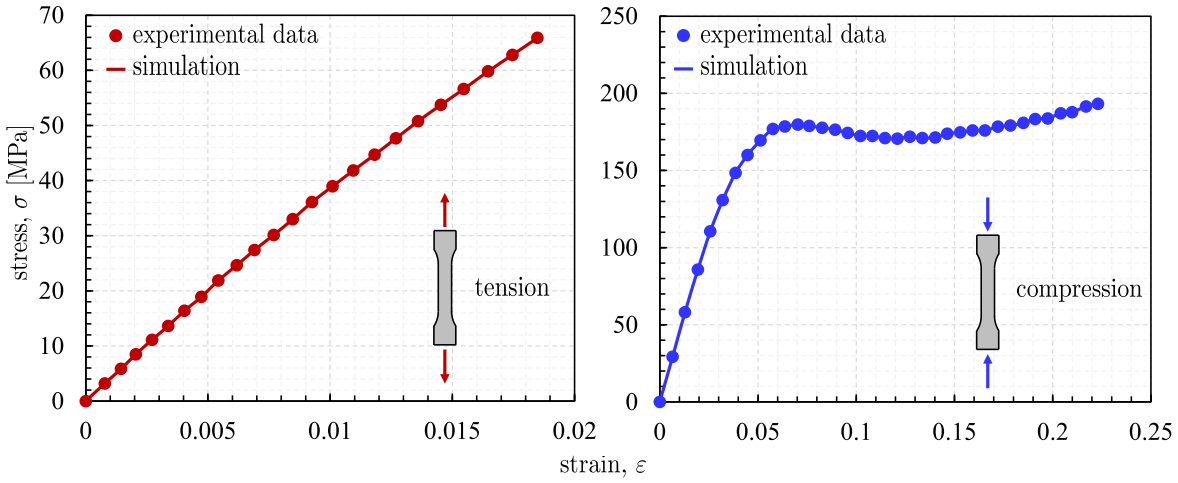

Fig. B.2. Calibration of the elasto-plastic model in tension and compression for Epoxy 3501-6.
Source: Experimental data taken from (Werner and Daniel, 2014).

where $\Delta\lambda$ is the increment of the plastic multiplier, subjected to the Kuhn–Tucker consistency conditions and to be updated via the return mapping algorithm. After a few algebraic manipulations, it is easy to show that:

$$\frac{\partial g_\sigma}{\partial \boldsymbol{\sigma}} = 3\boldsymbol{s} + \frac{2}{3}\alpha p \boldsymbol{\delta} \tag{B.4}$$

Substituting the foregoing equation in the non-associative flow rule, it is possible to find the following direct relationship for the plastic strain increment:

$$\Delta\boldsymbol{\epsilon}_p = \Delta\lambda\left(3\boldsymbol{s} + \frac{2}{3}\alpha p\boldsymbol{\delta}\right) \tag{B.5}$$

From the plastic strain increment, it is possible to define an equivalent plastic strain as follows:

$$\dot{\epsilon}^e_p = \sqrt{\frac{1}{1+2\nu_p^2}\dot{\boldsymbol{\epsilon}}_p : \dot{\boldsymbol{\epsilon}}_p} \tag{B.6}$$

which is used to link the hardening behavior of the polymer as characterized from uniaxial tests to the hardening in the presence of a general multiaxial stress state (Jirasek and Bazant, 2001). In this work, isotropic hardening is assumed with hardening equations for both tension and compression written in terms of the equivalent plastic strain $\sigma_{yt} = \sigma_{yt}\left(\epsilon^e_p\right)$, $\sigma_{yc} = \sigma_{yc}\left(\epsilon^e_p\right)$. Fig. B.2(a,b) show the uniaxial tension and compression curves utilized in this work to obtain the hardening laws. The symbols represent the experimental data provided in (Werner and Daniel, 2014) while the solid lines represent the fitting obtained by the proposed elasto-plastic model.

The model is implemented within an elastic predictor–plastic corrector algorithm (Belytschko et al., 2014). At the beginning of the $(n+1)$–th time increment, an initial trial stress is calculated assuming an elastic behavior:

$$\boldsymbol{\sigma}^{tr}_{n+1} = \boldsymbol{\sigma}_n + \boldsymbol{D}^e : \Delta\boldsymbol{\epsilon} \tag{B.7}$$

from which it is possible to extract the deviatoric and volumetric parts:

$$\begin{cases} \boldsymbol{s}^{tr}_{n+1} = \boldsymbol{s}_n + 2G\Delta\boldsymbol{e} & \text{(a)} \\ p^{tr}_{n+1} = p_n + K\Delta\epsilon_v & \text{(b)} \end{cases} \tag{B.8}$$

where ϵ_v = volumetric strain, $\boldsymbol{e}$ = deviatoric strain tensor, G = shear modulus, and K = bulk modulus.

After calculating the trial stress, the yielding condition is checked using the current tensile and compressive yield stresses. If $f_\sigma\left(\boldsymbol{\sigma}, \sigma_{yc}, \sigma_{yt}\right) < 0$ the material is still in the elastic regime and the trial stress can be considered as the correct stress: $\boldsymbol{\sigma}_{n+1} = \boldsymbol{\sigma}^{tr}_{n+1}$. On the other hand, if $f_\sigma\left(\boldsymbol{\sigma}, \sigma_{yc}, \sigma_{yt}\right) \geq 0$, the material has entered the plastic regime and the stress is not admissible. Hence, stresses and plastic strain must are recalculated to guarantee the yielding condition $f_\sigma\left(\boldsymbol{\sigma}, \sigma_{yc}, \sigma_{yt}\right) = 0$ using the closest point projection (Belytschko et al., 2014).

In addition to the curves shown in Fig. B.2(a,b), the other data used for the calibration of the model is $E = 4600$ GPa, $\nu = 0.35$. These properties were obtained from (Werner and Daniel, 2014).

B.0.1. Damage model

The combination of the damage model with the elasto-plastic model can be described by means of the following equation:

$$\boldsymbol{\sigma} = (1-\omega)\,\overline{\boldsymbol{\sigma}} = (1-\omega)\,\boldsymbol{D}_e : \left(\boldsymbol{\epsilon} - \boldsymbol{\epsilon}_p\right) \tag{B.9}$$

where ω is a scalar describing the amount of isotropic damage, $\boldsymbol{D}_e$ is the elastic stiffness, $\boldsymbol{\epsilon}$ is the total strain, $\boldsymbol{\epsilon}_p$ is the plastic strain, $\overline{\boldsymbol{\sigma}}$ is the effective stress and $\boldsymbol{\sigma}$ is the nominal stress. Eq. (B.9) underlies two different ways to combine stress-based plasticity with strain-based scalar damage. One possible approach is to have the plastic part expressed in terms of the effective stress (i.e. in the undamaged space). The other approach consists in having the plasticity part written in terms of the nominal stress (in the damage space). As was shown by Grassl and Jirásek in an excellent study (Grassl and Jirásek, 2006), only the first class of models provides local uniqueness without any restrictions on the model parameters. Accordingly, in this work, it was decided to have the plastic component of the model written in terms of the effective stress.

The evolution of the damage variable ω was calculated as a function of the equivalent plastic strain, ϵ^e_p, assuming a linear strain softening leading to the following expression:

$$\omega = 1 - \frac{\langle \epsilon^e_p - \epsilon^e_0 \rangle}{\epsilon^e_f - \epsilon^e_0} \tag{B.10}$$

In the foregoing equation, ϵ^e_0 is the equivalent plastic strain at damage initiation and ϵ^e_f is the equivalent plastic strain when the element is fully damaged. In the context of the crack band model (Bažant and Oh, 1983; Bažant and Planas, 1997; Bažant et al., 2021), the strain at complete failure must be adjusted as a function of the material fracture energy and the element size to guarantee a mesh-independent energy dissipation upon fracture:

$$\epsilon^e_f = \epsilon^e_0 + \frac{2G_f}{\sigma_y\left(\epsilon^e_0\right) h_e} - \frac{\sigma_y\left(\epsilon^e_0\right)}{E} \tag{B.11}$$

where $\sigma_y\left(\epsilon^e_0\right)$ is the yield stress at damage initiation, G_f is the fracture energy, and h_e is the characteristic length of the element. The crack

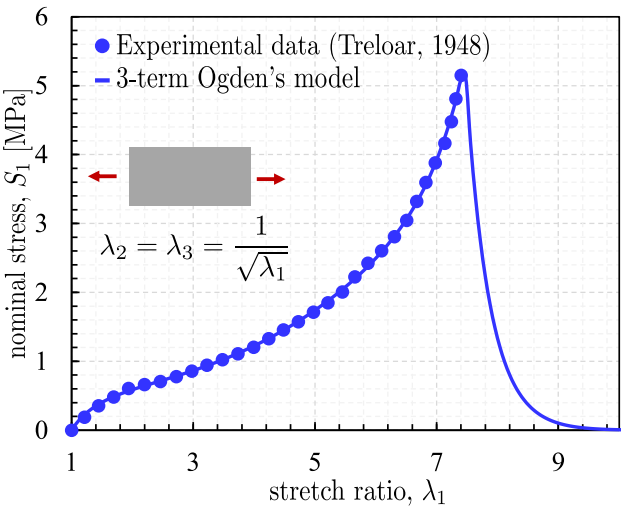

Fig. C.1. Uniaxial tensile behavior of the hyperelastic material considered in region Ω^A. The symbols represent data on vulcanized rubber taken from (Treloar, 1948). The solid line shows the fitting by the 3-term Ogden's model (Ogden, 1972). Note that the model has been modified to include strain softening using an improved version of the framework presented in (Volokh, 2007). Shown is the regularized softening curve for an element size of 0.3 mm using the crack band model (Bažant and Oh, 1983).

band model has been shown to accurately and objectively capture strain localization phenomena in a variety of materials including e.g. concrete (Bažant and Oh, 1983; Bažant et al., 2000; Caner and Bažant, 2013a,b), composites (Salviato et al., 2016b,a), and polymers (Qiao and Salviato, 2019a,b; Qiao et al., 2020). For the simulations performed in this work, the fracture energy was assumed to be $G_f = 1$ N/mm which is a typical value for epoxy polymers (Qiao and Salviato, 2019a). The elasto-plastic-damage model was implemented as a VUMAT subroutine in ABAQUS/Explicit.

Appendix C. Hyperelastic-damage model

In this work, the material in Ω^A is assumed to be vulcanized rubber. Considering the large deformations that can occur at the tip of the notch, a nearly-incompressible hyperelastic model was implemented with the strain energy density following a 3-term Ogden model (Ogden, 1972):

$$W = \sum_{i=1}^{3} \frac{2\mu_i}{\alpha_i^2}\left(\bar{\lambda}_1^{\alpha_i} + \bar{\lambda}_2^{\alpha_i} + \bar{\lambda}_3^{\alpha_i} - 3\right) + \frac{K}{2}(J-1)^2 \tag{C.1}$$

In the foregoing expression $\bar{\lambda}_i = \lambda_i / J^{1/3}$, λ_i with $i = 1...3$ are the stretch ratios, $J = \det(\boldsymbol{F})$ is the Jacobian, K is the bulk modulus for small deformations, and μ_i and α_i are material properties to be calibrated via experimental data. Starting from the strain energy density, the Cauchy stress tensor can be easily calculated as follows (Bower, 2009):

$$\boldsymbol{\sigma} = \frac{1}{J}\boldsymbol{F}\frac{\partial W}{\partial \boldsymbol{F}} \tag{C.2}$$

where $\boldsymbol{F}$ is the deformation gradient.

The strain energy density obtained from Eq. (C.1) increases indefinitely with increasing stretch ratios. Accordingly, it is not suitable to describe damage and fracture. To enable to capture strain softening a modified version of the strain energy function proposed in (Volokh, 2007) is used in this work:

$$\Psi(W) = \begin{cases} W & \text{for } W \le W_0 \quad \text{(a)} \\ W_0 + \Phi\left[1 - \exp\left(-\frac{W - W_0}{\Phi}\right)\right] & \text{for } W > W_0 \quad \text{(b)} \end{cases} \tag{C.3}$$

where W is calculated by means of Eq. (C.1), and W_0 and Φ are parameters that describe the softening behavior of the material. W_0 controls the damage initiation while Φ controls the initial slope of the softening curve. Following the crack band model (Bažant and Oh, 1983; Bažant and Planas, 1997; Bažant et al., 2021), these parameters must be adjusted as a function of the total fracture energy, G_f, and the element characteristic length, h_e.

Substituting Eqs. (C.3)(a) and (C.3)(b) into (C.2), the Cauchy stress tensor now reads:

$$\boldsymbol{\sigma} = \frac{1}{J}\boldsymbol{F}\frac{\partial W}{\partial \boldsymbol{F}} \exp\left(-\frac{\langle W - W_0\rangle}{\Phi}\right) \tag{C.4}$$

where $\langle x\rangle = \max(x, 0)$. Fig. C.1 shows the calibration of Eq. (C.4) using uniaxial tensile experimental data from (Treloar, 1948) using the Levenberg–Marquardt algorithm (Levenberg, 1944; Marquardt, 1963). As can be noted, Eq. (C.4) can accurately capture the experimental data with $\alpha_1 = 0.46$, $\alpha_2 = 15.81$, $\alpha_3 = 3.52$, $\mu_1 = 1.79$ MPa, $\mu_2 = 1.75 \times 10^{-13}$ MPa, $\mu_3 = 2.13 \times 10^{-2}$ MPa and $K = 2$ GPa. The figure also shows the exponential strain softening predicted by the hyperelastic model for an element size of 0.3 mm for which $W_0 = 1.22 \times 10^{-2}$ J/mm^3 and $\Phi = 1.00 \times 10^{-2}$ J/mm^3. For this work, the fracture energy was assumed to be $G_f = 3.7$ N/mm which is a typical value for vulcanized rubber.

The foregoing model was implemented as a VUMAT subroutine in ABAQUS/Explicit.

References

Abramowitz, M., Stegun, I.A., 1964. Handbook of Mathematical Functions with Formulas, Graphs, and Mathematical Tables, Vol. 55. US Government printing office.

Andrews, G.E., Askey, R., Roy, R., 1999. Special Functions. In: Encyclopedia of Mathematics and its Applications, vol. 71, Cambridge University Press, Cambridge.

Asp, L.E., Berglund, L.A., Gudmundson, P., 1995. Effects of a composite-like stress state on the fracture of epoxies. Compos. Sci. Technol. 53 (1), 27–37.

Asp, L., Berglund, L.A., Talreja, R., 1996. A criterion for crack initiation in glassy polymers subjected to a composite-like stress state. Compos. Sci. Technol. 56 (11), 1291–1301.

Bandyopadhyay, A., Heer, B., 2018. Additive manufacturing of multi-material structures. Mater. Sci. Eng. R 129, 1–16.

Bažant, Z.P., Caner, F.C., Carol, I., Adley, M.D., Akers, S.A., 2000. Microplane model M4 for concrete. I: Formulation with work-conjugate deviatoric stress. J. Eng. Mech. 126 (9), 944–953.

Bažant, Z.P., Le, J.-L., Salviato, M., 2021. Quasibrittle Fracture Mechanics and Size Effect. a First Course. Oxford University Press.

Bažant, Z.P., Oh, B.H., 1983. Crack band theory for fracture of concrete. Matériaux Construct. 16 (3), 155–177.

Bažant, Z.P., Planas, J., 1997. Fracture and Size Effect in Concrete and Other Quasibrittle Materials. CRC Press.

Belytschko, T., Liu, W.K., Moran, B., Elkhodary, K., 2014. Nonlinear finite elements for continua and structures. John wiley & sons.

Benzeggagh, M.L., Kenane, M., 1996. Measurement of mixed-mode delamination fracture toughness of unidirectional glass/epoxy composites with mixed-mode bending apparatus. Compos. Sci. Technol. 56 (4), 439–449.

Berto, F., Elices, M., Lazzarin, P., Zappalorto, M., 2012. Fracture behaviour of notched round bars made of PMMA subjected to torsion at room temperature. Eng. Fract. Mech. 90, 143–160.

Berto, F., Lazzarin, P., 2009. A review of the volume-based strain energy density approach applied to V-notches and welded structures. Theor. Appl. Fract. Mech. 52 (3), 183–194.

Bogy, D.B., 1971. Two edge-bonded elastic wedges of different materials and wedge angles under surface tractions. J. Appl. Mech. 38, 377–386.

Bower, A.F., 2009. Applied Mechanics of Solids. CRC Press.

Brown, J.W., Churchill, R.V., 2009. Complex Variables and Applications Eighth Edition. McGraw-Hill Book Company.

Canal, L.P., Segurado, J., LLorca, J., 2009. Failure surface of epoxy-modified fiber-reinforced composites under transverse tension and out-of-plane shear. Int. J. Solids Struct. 46 (11–12), 2265–2274.

Caner, F.C., Bažant, Z.P., 2013a. Microplane model M7 for plain concrete. I: Formulation. J. Eng. Mech. 139 (12), 1714–1723.

Caner, F.C., Bažant, Z.P., 2013b. Microplane model M7 for plain concrete. II: Calibration and verification. J. Eng. Mech. 139 (12), 1724–1735.

Christensen, R.M., 2013. The Theory of Materials Failure. Oxford University Press.

Driscoll, T.A., Trefethen, L.N., 2002. Schwarz-Christoffel Mapping, Vol. 8. Cambridge University Press.

Fisher, S.D., 1999. Complex Variables. Dover Publications, Inc..
González, C., LLorca, J., 2007. Mechanical behavior of unidirectional fiber-reinforced polymers under transverse compression: microscopic mechanisms and modeling. Compos. Sci. Technol. 67 (13), 2795–2806.
Grassl, P., Jirásek, M., 2006. Damage-plastic model for concrete failure. Int. J. Solids Struct. 43 (22–23), 7166–7196.
Gross, B., Mendelson, A., 1972. Plane elastostatic analysis of V-notched plates. Int. J. Fract. Mech. 8 (3), 267–276.
Hein, V., Erdogan, F., 1971. Stress singularities in a two-material wedge. Int. J. Fract. Mech. 7 (3), 317–330.
Hu, Y., Xia, Z., Ellyin, F., 2003. Deformation behavior of an epoxy resin subject to multiaxial loadings. part I: Experimental investigations. Polym. Eng. Sci. 43 (3), 721–733.
Irwin, G.R., 1958. Fracture. In: Fl"ugge, S. (Ed.), Handbuch Der Physik, Vol. 6. Spinger-Verlag, Berlin, pp. 551–590.
Jirasek, M., Bazant, Z.P., 2001. Inelastic Analysis of Structures. John Wiley & Sons.
Kumagai, Y., Onodera, S., Salviato, M., Okabe, T., 2020. Multiscale analysis and experimental validation of crack initiation in quasi-isotropic laminates. Int. J. Solids Struct. 193, 172–191.
Lazzarin, P., Berto, F., Gomez, F., Zappalorto, M., 2008. Some advantages derived from the use of the strain energy density over a control volume in fatigue strength assessments of welded joints. Int. J. Fatigue 30 (8), 1345–1357.
Lazzarin, P., Zambardi, R., 2001. A finite-volume-energy based approach to predict the static and fatigue behavior of components with sharp V-shaped notches. Int. J. Fract. 112 (3), 275–298.
Le, J.-L., Bažant, Z.P., Yu, Q., 2010. Scaling of strength of metal-composite joints—part II: Interface fracture analysis. J. Appl. Mech. 77 (1).
Levenberg, K., 1944. A method for the solution of certain non-linear problems in least squares. Quart. Appl. Math. 2 (2), 164–168.
Lin, E., Li, Y., Weaver, J.C., Ortiz, C., Boyce, M.C., 2014. Tunability and enhancement of mechanical behavior with additively manufactured bio-inspired hierarchical suture interfaces. J. Mater. Res. 29 (17), 1867–1875.
Marquardt, D.W., 1963. An algorithm for least-squares estimation of nonlinear parameters. J. Soc. Ind. Appl. Math. 11 (2), 431–441.
Martin, J.J., Fiore, B.E., Erb, R.M., 2015. Designing bioinspired composite reinforcement architectures via 3D magnetic printing. Nature Commun. 6 (1), 1–7.
Neuber, H., 1958a. Kerbspannungslehre. Springer-Verlag, Berlin, German.
Neuber, H., 1958b. Theory of Notch Stresses: Principles for Exact Stress Calculation. AEC TR 4547.
Ogden, R.W., 1972. Large deformation isotropic elasticity–on the correlation of theory and experiment for incompressible rubberlike solids. Proc. R. Soc. Lond. Ser. A Math. Phys. Eng. Sci. 326 (1567), 565–584.
Pastrello, M., Salviato, M., Zappalorto, M., 2022. Stress distributions in orthotropic solids with blunt notches under in-plane shear loadings. Eur. J. Mech. A Solids 92, 104436.
Poulain, X., Benzerga, A., Goldberg, R., 2014. Finite-strain elasto-viscoplastic behavior of an epoxy resin: Experiments and modeling in the glassy regime. Int. J. Plast. 62, 138–161.
Qiao, Y., Salviato, M., 2019a. Strength and cohesive behavior of thermoset polymers at the microscale: A size-effect study. Eng. Fract. Mech. 213, 100–117.
Qiao, Y., Salviato, M., 2019b. Study of the fracturing behavior of thermoset polymer nanocomposites via cohesive zone modeling. Compos. Struct. 220, 127–147.
Qiao, Y., Zhang, Q., Salviato, M., 2020. Effects of in-situ stress state on the plastic deformation, fracture, and size scaling of thermoset polymers and related fiber-reinforced composites. In: ASC 35th Technical Conference, No. July.
Rafiee, M., Farahani, R.D., Therriault, D., 2020. Multi-material 3D and 4D printing: a survey. Adv. Sci. 7 (12), 1902307.
Raghava, R., Caddell, R.M., Yeh, G.S., 1973. The macroscopic yield behaviour of polymers. J. Mater. Sci. 8 (2), 225–232.
Raney, J.R., Compton, B.G., Mueller, J., Ober, T.J., Shea, K., Lewis, J.A., 2018. Rotational 3D printing of damage-tolerant composites with programmable mechanics. Proc. Natl. Acad. Sci. 115 (6), 1198–1203.
Salviato, M., Ashari, S.E., Cusatis, G., 2016a. Spectral stiffness microplane model for damage and fracture of textile composites. Compos. Struct. 137, 170–184.
Salviato, M., Kirane, K., Ashari, S.E., Bažant, Z.P., Cusatis, G., 2016b. Experimental and numerical investigation of intra-laminar energy dissipation and size effect in two-dimensional textile composites. Compos. Sci. Technol. 135, 67–75.
Salviato, M., Phenisee, S.E., 2019. Enhancing the electrical and thermal conductivities of polymer composites via curvilinear fibers: An analytical study. Math. Mech. Solids 24 (10), 3231–3253.
Salviato, M., Zappalorto, M., 2016. A unified solution approach for a large variety of antiplane shear and torsion notch problems: Theory and examples. Int. J. Solids Struct. 102, 10–20.
Salviato, M., Zappalorto, M., Maragoni, L., 2018. Exact solution for the mode III stress fields ahead of cracks initiated at sharp notch tips. Eur. J. Mech. A Solids 72, 88–96.
Sokolnikoff, I.S., 1956. Mathematical Theory of Elasticity. McGraw-Hill New York.
Sugiyama, K., Matsuzaki, R., Malakhov, A.V., Polilov, A.N., Ueda, M., Todoroki, A., Hirano, Y., 2020. 3D Printing of optimized composites with variable fiber volume fraction and stiffness using continuous fiber. Compos. Sci. Technol. 186, 107905.
Suksangpanya, N., Yaraghi, N.A., Pipes, R.B., Kisailus, D., Zavattieri, P., 2018. Crack twisting and toughening strategies in bouligand architectures. Int. J. Solids Struct. 150, 83–106.
Suzuki, K., Phenisee, S.E., Salviato, M., 2021. An isogeometric framework for the modeling of curvilinear anisotropic media. Compos. Struct. 266, 113771.
Treloar, L., 1948. Stresses and birefringence in rubber subjected to general homogeneous strain. Proc. Phys. Soc. (1926-1948) 60 (2), 135.
Tschoegl, N., 1971. Failure surfaces in principal stress space. In: Journal of Polymer Science Part C: Polymer Symposia, Vol. 32. Wiley Online Library, pp. 239–267.
Ubaid, J., Wardle, B.L., Kumar, S., 2018. Strength and performance enhancement of multilayers by spatial tailoring of adherend compliance and morphology via multimaterial jetting additive manufacturing. Sci. Rep. 8 (1), 1–10.
Volokh, K., 2007. Hyperelasticity with softening for modeling materials failure. J. Mech. Phys. Solids 55 (10), 2237–2264.
Werner, B., Daniel, I., 2014. Characterization and modeling of polymeric matrix under multi-axial static and dynamic loading. Compos. Sci. Technol. 102, 113–119.
Xia, Z., Hu, Y., Ellyin, F., 2003. Deformation behavior of an epoxy resin subject to multiaxial loadings. Part II: Constitutive modeling and predictions. Polym. Eng. Sci. 43 (3), 734–748.
Yoshida, M., 2013. Hypergeometric Functions, my Love: Modular Interpretations of Configuration Spaces. Springer Science & Business Media, Berlin.
Yu, Q., Bažant, Z.P., Bayldon, J., Le, J.-L., Caner, F.C., Ng, W.H., Waas, A.M., Daniel, I.M., 2010. Scaling of strength of metal-composite joints—Part I: Experimental investigation. J. Appl. Mech. 77 (1).
Zaheri, A., Fenner, J.S., Russell, B.P., Restrepo, D., Daly, M., Wang, D., Hayashi, C., Meyers, M.A., Zavattieri, P.D., Espinosa, H.D., 2018. Revealing the mechanics of helicoidal composites through additive manufacturing and beetle developmental stage analysis. Adv. Funct. Mater. 28 (33), 1803073.
Zappalorto, M., Lazzarin, P., 2011. In-plane and out-of-plane stress field solutions for V-notches with end holes. Int. J. Fract. 168 (2), 167–180.
Zappalorto, M., Lazzarin, P., Yates, J., 2008. Elastic stress distributions for hyperbolic and parabolic notches in round shafts under torsion and uniform antiplane shear loadings. Int. J. Solids Struct. 45 (18–19), 4879–4901.
Zappalorto, M., Salviato, M., 2019. Antiplane shear stresses in orthotropic plates with lateral blunt notches. Eur. J. Mech. A Solids 77, 103815.
Zappalorto, M., Salviato, M., Maragoni, L., 2019. Analytical study on the mode III stress fields due to blunt notches with cracks. Fatigue Fract. Eng. Mater. Struct. 42 (3), 612–626.